The Impact of a Prominent Rain Shadow on Flooding in California's Santa Cruz Mountains: A CALJET Case Study and Sensitivity to the ENSO Cycle

F. MARTIN RALPH AND PAUL J. NEIMAN

NOAA/Environmental Technology Laboratory, Boulder, Colorado

DAVID E. KINGSMILL

Desert Research Institute, Reno, Nevada

P. OLA G. PERSSON AND ALLEN B. WHITE

Cooperative Institute for Research in Environmental Sciences/NOAA/ETL, Boulder, Colorado

ERIC T. STREM

NOAA/National Weather Service/California–Nevada River Forecast Center, Sacramento, California

EDMUND D. ANDREWS AND RONALD C. ANTWEILER

U.S. Geological Survey, Boulder, Colorado

(Manuscript received 9 August 2002, in final form 9 May 2003)

ABSTRACT

Data from the California Land-Falling Jets Experiment (CALJET) are used to explore the causes of variations in flood severity in adjacent coastal watersheds within the Santa Cruz Mountains on 2–3 February 1998. While Pescadero Creek (rural) experienced its flood of record, the adjacent San Lorenzo Creek (heavily populated), attained only its fourth-highest flow. This difference resulted from conditions present while the warm sector of the storm, with its associated low-level jet, high moisture content, and weak static stability, was overhead. Rainfall in the warm sector was dominated by orographic forcing. While the wind speed strongly modulated rain rates on windward slopes, the wind direction positioned the edge of a rain shadow cast by the Santa Lucia Mountains partially over the San Lorenzo basin, thus protecting the city of Santa Cruz from a more severe flood. Roughly 26% ± 9% of the streamflow at flood peak on Pescadero Creek resulted from the warm-sector rainfall. Without this rainfall, the peak flow on Pescadero Creek would likely not have attained record status.

These results are complemented by a climatological analysis based on ~50-yr-duration streamflow records for these and two other nearby windward watersheds situated ~20 to 40 km farther to the east, and a comparison of this climatological analysis with composites of NCEP–NCAR reanalysis fields. The westernmost watersheds were found to have their greatest floods during El Niño winters, while the easternmost watersheds peaked during non–El Niño episodes. These results are consistent with the case study, that showed that the composite 925-mb, meridionally oriented wind direction during El Niños favors a rain shadow over the eastern watersheds. During non–El Niño periods, the composite, zonally oriented wind direction indicates that the sheltering effect of the rain shadow on the eastern watersheds is reduced, while weaker winds, less water vapor, and stronger stratification reduce the peak runoff in the western watersheds relative to El Niño periods.

These case study and climatological results illustrate the importance of conditions in the moisture-rich warm sector of landfalling Pacific winter storms. Although many other variables can influence flooding, this study shows that variations of ±10° in wind direction can modulate the location of orographically enhanced floods. While terrain can increase predictability (e.g., rainfall typically increases with altitude), the predictability is reduced when conditions are near a threshold separating different regimes (e.g., in or out of a rain shadow).

Corresponding author address: Dr. F. Martin Ralph, NOAA/Environmental Technology Laboratory, Mail Code R/ET7, 325 Broadway, Boulder, CO 80305.
E-mail: Marty.Ralph@noaa.gov

1. Introduction

On 2–3 February 1998, during one of the strongest El Niño episodes of the twentieth century (e.g., Barnston et al. 1999), a major extratropical cyclone struck California. Several hours before the heaviest rainfall [which was associated with a low-level jet (LLJ) and primary cold front] reached California's central coast, precise measurements of the LLJ intensity were gathered offshore by a National Oceanic and Atmospheric Administration (NOAA) P-3 aircraft and were communicated to the local National Weather Service (NWS) Weather Forecast Office (WFO) in Monterey. The offshore observation of a 37 m s^{-1} LLJ (Fig. 1) was collected as part of an experimental storm surveillance effort within the California Land-Falling Jets Experiment (CALJET; Ralph et al. 1999).[1] This measurement confirmed forecasters' concerns about the potential for flooding during the storm's landfall (e.g., Neiman et al. 2002), and led to the issuance of a flash flood warning more than 6 h before flood stage was reached on local watersheds, including Pescadero Creek (Figs. 1 and 2). Emergency managers credited the unusual length of this lead time (which is normally ≤1 h) with their ability to preposition personnel for the many rescues carried out that evening (T. Maruyama, Director of Emergency Services, San Mateo County Sheriff's Office, 1998, personal communication). A retrospective assessment by these managers revealed that the lead time saved both lives and property.

Rainfall totals reached 350 mm in 45 h in the coastal mountains and led to major flooding that varied significantly from one watershed to the next. This variability modulated societal impacts in the Santa Cruz Mountains (Figs. 1, 2) because the worst flooding struck the sparsely populated Pescadero Creek basin (record flood; population ~1500) rather than the adjacent, densely populated San Lorenzo Creek basin that flows through the city of Santa Cruz (fourth-worst flood, population ~75 000). Although both watersheds had significant flooding, and the flood warning helped emergency managers, it is important to consider whether predictability is available on a scale that would further distinguish which watersheds may be the most vulnerable in a particular event.

This paper describes the causes of local-scale variations in rainfall that led to the flooding, including the circumstances that led to the record flood on Pescadero Creek. The paper focuses on orographic effects (e.g., Smith 1979; Houze 1993), including precipitation enhancement associated with the landfall of a LLJ in the warm sector of the cyclone (i.e., the region between the warm front and leading cold front), and the role of a distinct rain shadow (e.g., Brady and Waldstreicher
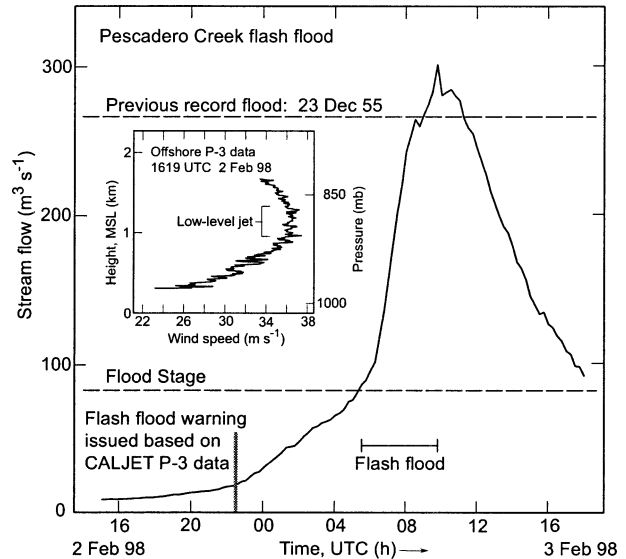
---

[1] Key elements of CALJET's data collection were expanded due to the strong El Niño.

FIG. 1. Time series of streamflow (m^3 s^{-1}) from the Pescadero Creek stream gauge between 1500 UTC 2 Feb and 1800 UTC 3 Feb 1998. A NOAA P-3 aircraft observed hurricane-force winds offshore (inset) within a moist low-level jet in the cyclone warm sector (i.e., near the 1600 UTC flight-track label in Fig. 4a) later.

2001). The importance of warm-sector rainfall to total rainfall in landfalling winter storms was noted by Reynolds and Kuciauskas (1988) and Heggli and Rauber (1988), and was part of the basis for CALJET's focus on the LLJ. A key factor addressed in this study is the strong sensitivity of flooding to wind direction in the LLJ. [This sensitivity is reflected in the use of 10° wind-direction bins in the Rhea (1978) operational orographic precipitation algorithm.] This paper extends earlier studies through use of wind profiler and aircraft data gathered during CALJET (Ralph et al. 1999), and benefits from the proximity of a Weather Surveillance Radar-1988 Doppler (WSR-88D) that overlooks both watersheds at ranges from only 8 to 50 km. This case study also reveals details of the capabilities and limitations of coastal WSR-88D radars (Westrick et al. 1999) and wind profilers in terms of monitoring key conditions in landfalling storms, and reveals the influence of topography on local-scale predictability of precipitation.

The conclusions of this case study are then used to explore the connection between local flooding variability and larger-scale conditions influenced by the El Niño–Southern Oscillation (ENSO). Watershed-scale sensitivity to ENSO was established by Andrews et al. (2004), which analyzed flooding as a function of ENSO for key coastal watersheds in California. The study presented here connects extreme weather to short-term climate variations by describing how a key mesoscale process that governs the local distribution of coastal winter rainfall in California is modulated by ENSO. These results have implications for understanding how topography influences the predictability of precipitation in
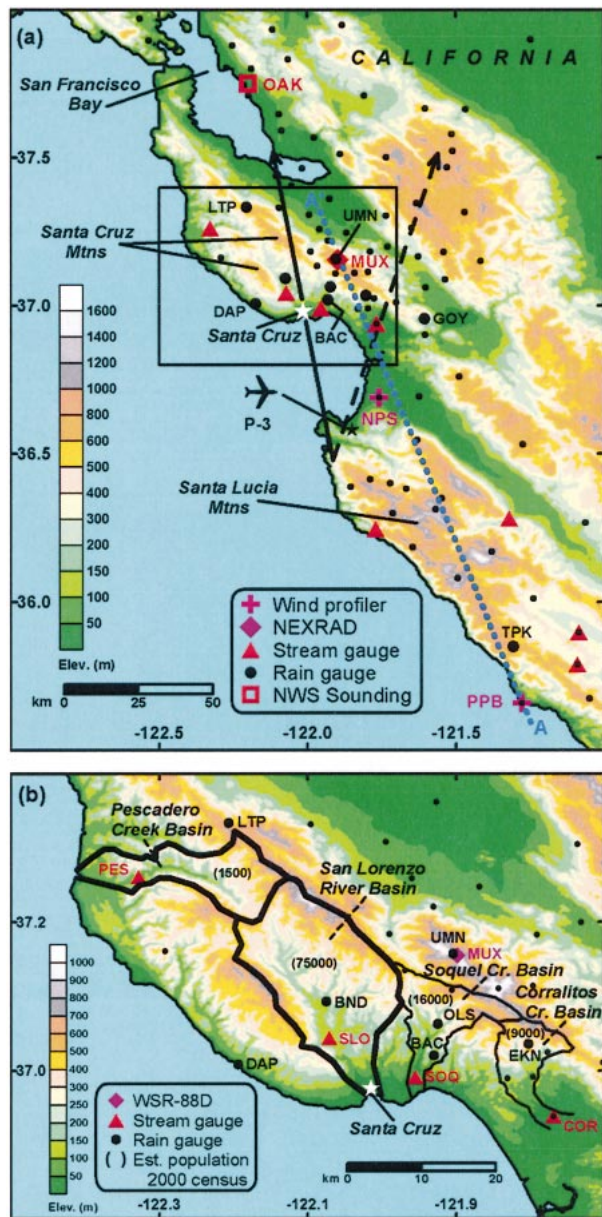
FIG. 2. (a) Terrain base map of CA central-coast region showing the locations of the observing systems (see key) and the NOAA P-3 aircraft staging area at Monterey (aircraft symbol). Rain gauge sites whose data are presented in time series format later in the paper are denoted with large dots. Dividing streamlines directed from 169° and 199° (solid and dashed, respectively) are shown. Dotted-line AA′ is a cross-section projection for Fig. 11b. The inset box defines the domain of (b) and Fig. 13. Zoomed-in terrain base map showing the observing systems [as in (a)], the outlines of the four watersheds of interest, and the estimated populations within these watersheds. Observing sites key to our discussion are depicted by their three-letter station names. The Pescadero and San Lorenzo watershed boundaries are bold.

mountains. This is an area of debate (e.g., Smith et al. 1997) about the role of terrain in increasing predictability (Charba et al. 2003) versus increasing uncertainty when meteorological conditions are close to a key hydrodynamic threshold. In such situations, small changes in upstream conditions can yield large changes in flow regime. The results of Nuss and Miller (2001), which concluded ±1° changes in the large-scale wind-direction field can create large local errors in wind and precipitation forecasts in complex terrain, support this later view.

2. Observing systems

During the winter of 1997/98, an extensive suite of research observing platforms, some of which were mobile, was deployed for CALJET across a region covering the data-sparse eastern Pacific Ocean and coastal California (Ralph et al. 1999). These platforms complemented the established operational observing systems. Those research and operational systems that are critical to this study are described briefly in the following paragraphs and their locations are shown in Fig. 2.

Key ground-based data were collected from two 915-MHz boundary layer wind profilers (e.g., Ecklund et al. 1988) (Fig. 2a), including one operated by the Naval Postgraduate School (NPS). The other was sited near Point Piedras Blancas (PPB) on the coast. This site, and 11 others (Fig. 4), were deployed by NOAA's Environmental Technology Laboratory (ETL) from Oregon to southern California for winter weather and air quality research. All of these profilers provided hourly averaged vertical profiles of horizontal wind velocity from ∼0.1 to 4.0 km above ground level (AGL) with ≤100 m vertical resolution in clear, cloudy, and precipitating conditions. Under dry conditions the height coverage could drop to 2.0 km AGL. The ETL profiler winds were objectively edited using the method of Weber et al. (1993). At each profiler site a tipping-bucket rain gauge measured rainfall with 0.01-in. (∼0.25 mm) resolution, while observations of wind, temperature, moisture, and pressure were collected from a 10-m tower, all with 2-min sampling.

Data gathered offshore by a NOAA P-3 turboprop research aircraft (e.g., Jorgensen 1984; Jorgensen et al. 1996) allowed accurate determination of the positions and structure of fronts and the LLJ offshore as the storm approached the coast on 2 February 1998. This flight started from Monterey, California, reached ∼375 mb altitude, and released nine global-positioning-system (GPS) dropsondes. The sondes provided high-resolution vertical profiles of wind velocity, temperature, and water vapor over the data-sparse Pacific Ocean. The next part of the mission focused on low-altitude flight legs in the LLJ and ended with a leg near the coast. The P-3 also provided airborne dual-Doppler radar measurements (not shown) of the offshore fronts and LLJ, which aided the synoptic analyses (Fig. 3).
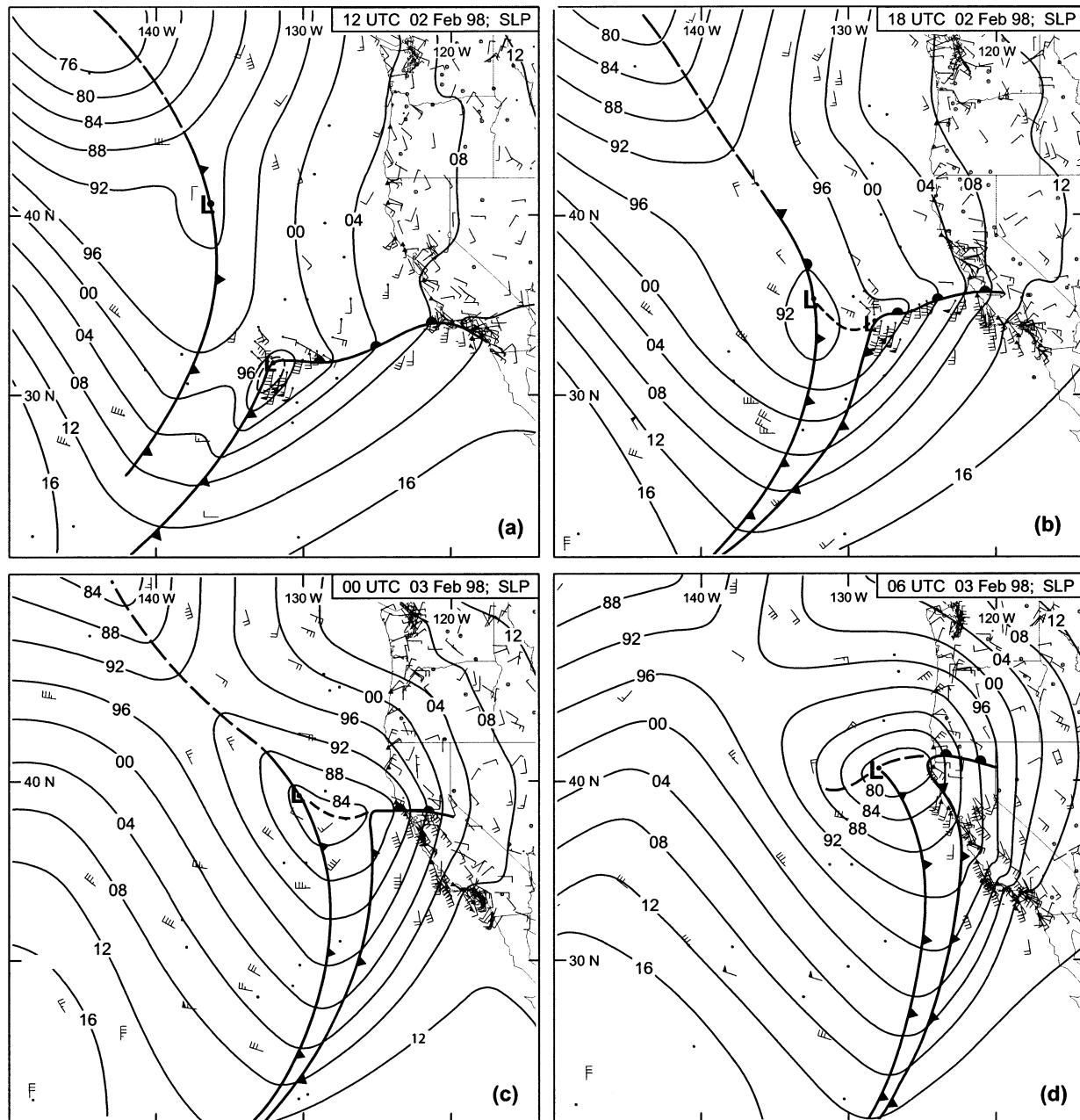
FIG. 3. Sea level pressure (SLP) analysis at (a) 1200 UTC and (b) 1800 UTC 2 Feb; (c) 0000 UTC and (d) 0600 UTC 3 Feb 1998. Surface wind flags are 25 m s^{-1}, full barbs are 5 m s^{-1}, and half-barbs are 2.5 m s^{-1}. The ocean-based observations are from ships and buoys [no vector heads or stand-alone solid dots (SLP-only reports)], and from P-3 dropsondes and low-level flight legs (dot vector heads). Wind-profiler sites have triangle vector heads. Standard frontal notation is used.

Operational observing systems were also vital. California's Automated Local Evaluation in Real Time (ALERT; Mendell 1992) network of ~900 rain gauges measured rainfall with 0.04-in. (~1.0 mm) resolution as frequently as every 15 min, and were quality controlled. Data from eight United States Geological Survey (USGS) stream gauges in the Santa Cruz and Santa Lucia Mountains were used in the climatological part of the study. These gauges were well suited for this study because the watersheds they represent are relatively small, not subjected to flow regulation, and low enough in altitude (<1500 m) that most precipitation falls as rain. All of the stream gauges in the Santa Cruz Mountains have 45–50 yr of records dating back to between 1950 and 1955.

Many other operational observing systems were also used: hourly surface observations from airports and buoys, 3-hourly data from ships (sites shown in Fig. 3),

12-hourly thermodynamic and kinematic profiles from rawinsondes, and the WSR-88D at Mount Umunhum (MUX) near San Francisco monitored the evolution of landfalling precipitation features and their associated radial-velocity signatures over the domain of interest. General descriptions and applications of WSR-88D are provided in Crum et al. (1993) and Klazura and Imy (1993). The WSR-88D radial velocities were synthesized into vertical profiles of the horizontal wind with ~300 m vertical resolution using the velocity–azimuth display (VAD) technique (Browning and Wexler 1968; Rabin and Zrnić 1980). A Geostationary Operational Environmental Satellite (GOES) provided continuous infrared, visible, and water-vapor observations, as well as 3-hourly tropospheric-feature-tracked winds (e.g., Velden et al. 1997; Nieman et al. 1997). A polar-orbiting satellite measured integrated precipitable water vapor (IWV), surface wind speed, integrated cloud liquid water, and rain rate in >1000-km-wide swaths over the Pacific Ocean with its Special Sensor Microwave Imager (SSM/I) instrument (Wentz 1997).

3. Synoptic overview and areawide rainfall distribution on 2–3 February 1998

The CALJET winter of 1997/98 coincided with a high-amplitude El Niño event and was characterized by frequent and strong storms impacting the California coast (e.g., NCDC 1998). One of the strongest storms occurred on 2–3 February 1998, causing hurricane-force winds, extensive flooding, landslides, and coastal erosion. The synoptic evolution of this frontal cyclone over the eastern Pacific Ocean is presented to establish the large-scale context for the mesoscale and hydrological observations and analyses explored later in the paper. The sea level pressure (SLP) analyses (Fig. 3) were derived largely from ship and buoy observations over the ocean and from land-based observations. Flight-level and dropsonde data from NOAA's P-3 aircraft on 2 February refined the analyses at 1200 and 1800 UTC over the data-sparse eastern Pacific. GOES-retrieved winds (shown in Fig. 4), and the SSM/I products, provided additional constraints. Surface frontal positions were based on surface time series traces, cross sections constructed from the rawinsondes and the P-3, coastal wind-profiler data, and satellite-derived products. (For brevity, the cross sections and sounding analyses are not shown.) A meso-α-scale snapshot of this storm along the California coast during a key period is shown (Fig. 5), followed by an accumulated rainfall analysis (Fig. 6).

The SLP analyses and infrared satellite imagery from 1200 UTC 2 February to 0600 UTC 3 February (Figs. 3, 4) show an evolving frontal wave with conjoined cold and warm fronts situated east of a trailing cold front. The storm's cloud field remained somewhat disorganized, never acquiring a classical wrapped-up comma-cloud configuration typical of intense cyclones. Baro-

clinic cloud-leaf development associated with a warm conveyor belt (e.g., Carlson 1991) coincided with the frontal wave, and the evolving but ill-defined comma head marked the location of a deep-tropospheric polar vortex and the eventual surface cyclone position. Lower-tropospheric feature-tracked winds could not be retrieved in the heart of the storm environment because of high clouds.

The storm had a complex structure and evolution. Between 1200 and 1800 UTC 2 February (Figs. 3a–b), the P-3 documented a mesoscale cyclone that rapidly developed and then decayed at the cusp of the frontal wave offshore of California. Thereafter (Figs. 3b–d), cyclogenesis occurred along the trailing cold front over the open waters. The P-3 also recorded (not shown) complex thermodynamic and kinematic structures, including the presence of multiple cold fronts, as seen in another coastal storm (Chien et al. 2001). The P-3 data also confirmed the presence of a LLJ (~37 m s^{-1} at 1 km MSL) transporting subtropical moisture (mixing ratio >10 g kg^{-1}) northward ahead of the leading cold front in the frontal wave's warm sector. This wave struck California on 2 and 3 February (Figs. 3 and 4) and was primarily responsible for the severe weather problems on the coast.

On the meso-α-scale (Fig. 5), the subtropical warm sector covered most of California at 0330 UTC 3 February, as the warm front moved northward toward Oregon and the leading cold front approached California from the west. Synoptic-scale forcing was weak in the warm sector relative to these flanking frontal regions. Coastal wind-profiler observations at 1000 m MSL clearly resolved a south-southeasterly low-level jet (25–33 m s^{-1}) ahead of the leading cold front. A fortuitous SSM/I overpass at 0348 UTC covered the entire coastal zone and documented the IWV distribution in the storm environment. A plume of IWV exceeding 3 cm roughly paralleled the leading cold front on its warm side, and a local maximum of >4 cm was situated where the record flood in Pescadero Creek occurred in the western Santa Cruz Mountains 6 h later. It should be noted that the reliability of IWV retrievals is reduced in rain (e.g., Wentz 1997), and within ~25 km of the coast. Because the area of ≥4 cm IWV extended >100 km offshore (Fig. 5), it likely reflected a true local maximum.

An analysis of accumulated rainfall from the 45-h period between 0300 UTC 2 February and 0000 UTC 4 February 1998 is shown for California's central coast (Fig. 6). The most striking characteristic of this analysis is the heavy rain that fell in the coastal mountains, thus implying that orographic forcing contributed significantly to the rainfall in the higher terrain. The Santa Lucia Mountains were inundated with 200–350 mm, and the Santa Cruz Mountains received >150 mm (determined, in part, using radar reflectivity data—see section 5b). Prominent rainfall minima, or rain shadows, were observed downstream (i.e., NE) of the Santa Lucia and Santa Cruz Mountains.
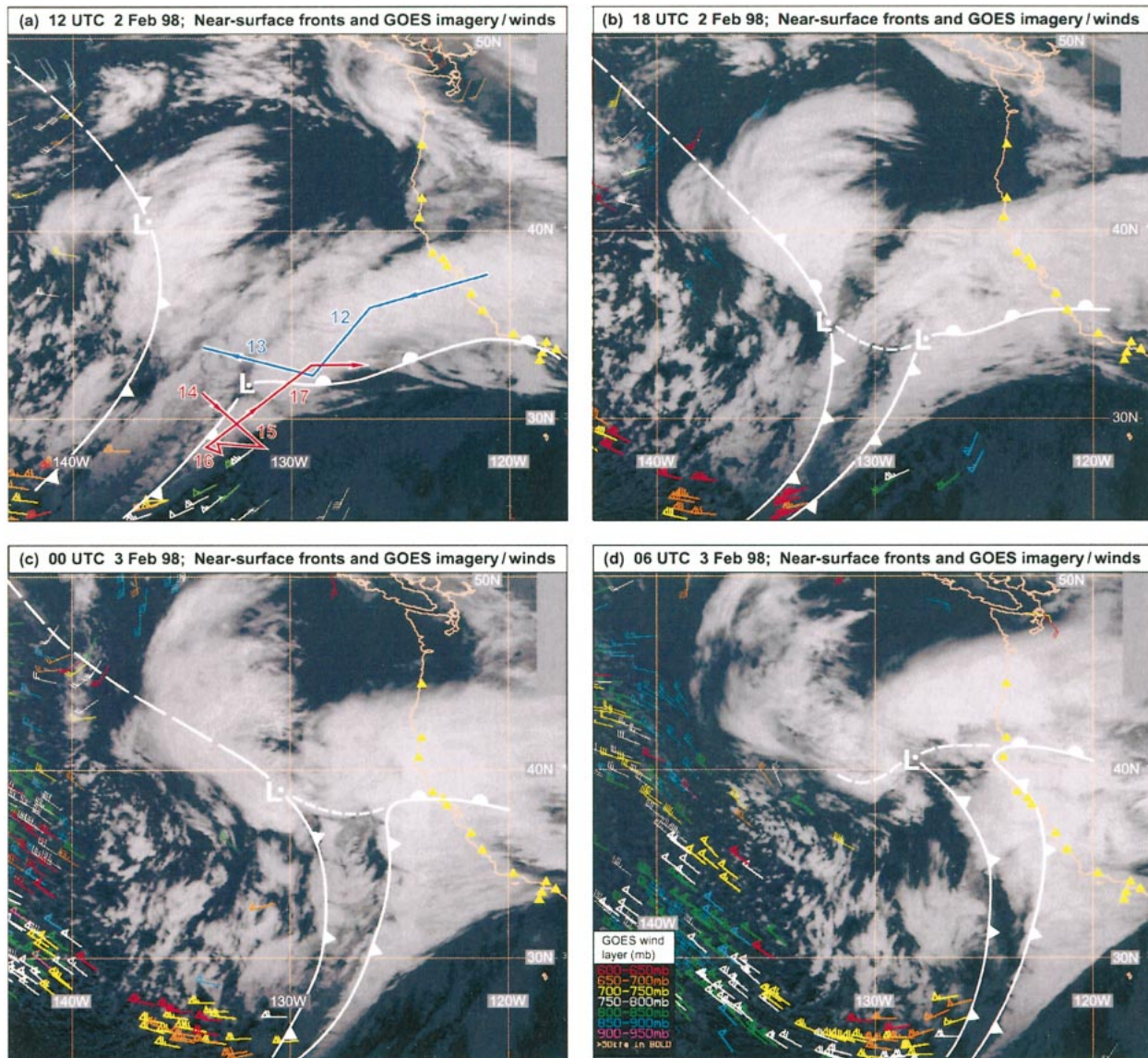
FIG. 4. NOAA GOES infrared satellite images with frontal positions at (a) 1200 UTC and (b) 1800 UTC 2 Feb; and (c) 0000 UTC and (d) 0600 UTC 3 Feb 1998. Satellite-derived feature-tracked winds below 600 mb are shown [wind flags and barbs are as in Fig. 3; color-coded key in (d)]. The coastal wind-profiler array is defined by the string of triangles along the West Coast. Panel (b) includes P-3 flight legs time-to-space adjusted to 1200 UTC 2 Feb: blue line, upper-level leg (~400 mb); red line, low-level leg (below 850 mb).

4. Rainfall and hydrological observations in adjacent watersheds

This section describes the rainfall and flooding that was observed during the 2–3 February storm in four adjacent watersheds on the southwestern flank of the Santa Cruz Mountains through four key stream gauges [i.e., Pescadero (PES), San Lorenzo (SLO), Soquel (SOQ), and Corralitos (COR); see Fig. 2b for locations]. Rainfall and streamflow traces from each of these watersheds are shown (Figs. 7 and 8). These traces are from a rain gauge and a stream gauge in the upper and

lower portion of each watershed, respectively.[2] To place these observations in the proper meteorological context, annotations highlight the surface passage of the warm front and the narrow cold-frontal rainband (NCFR; e.g., Parsons 1992) associated with the leading cold front. The time between the warm front and NCFR represents

---

[2] Because there were no usable rain gauges in the upper Pescadero Creek watershed during this event, the nearest gauge (LTP; see Fig. 2 for location) was used. Reflectivity data from the MUX WSR-88D radar showed that the LTP trace reasonably represented rainfall in the upper Pescadero watershed.
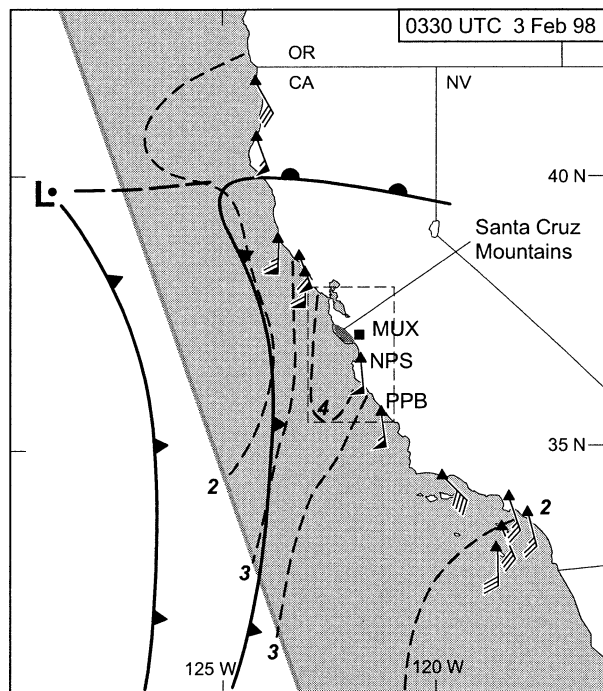
FIG. 5. Wind-profiler observations at 1000 m MSL (wind flags and barbs are as in Fig. 3), and interpolated surface frontal positions, at 0330 UTC 3 Feb 1998. The SSM/I overpass (gray-shaded swath) at 0348 UTC: dashed contours, vertically integrated precipitable water vapor (cm). The wind profilers (PPB, NPS) and WSR-88D radar (MUX) within the inset domain are labeled; this domain is used in Figs. 2a and 6.
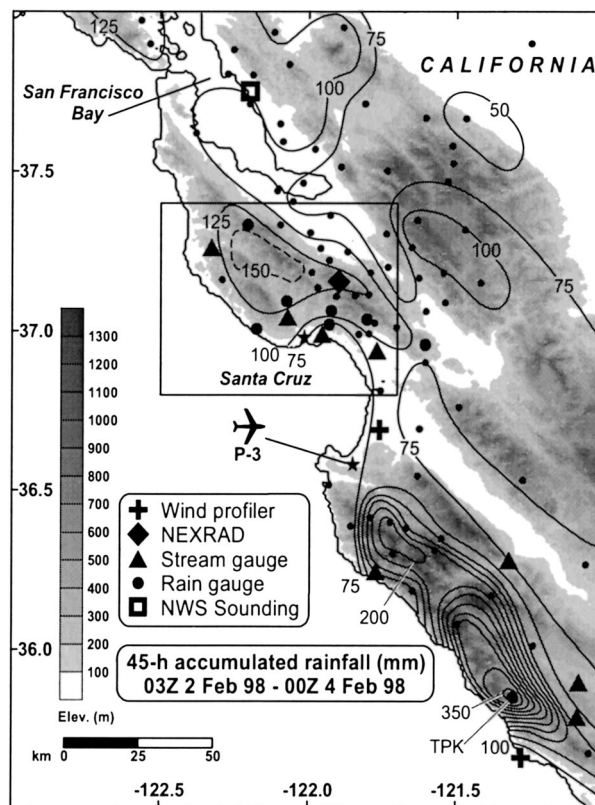

FIG. 6. Terrain base map showing the observing systems [as in Fig. 2(a)] and a 45-h accumulated rainfall analysis (mm) between 0300 UTC 2 Feb and 0000 UTC 4 Feb 1998. The dashed 150-mm contour over the Santa Cruz Mountains is an estimate of the rainfall based partly on radar reflectivity observations from MUX. The inset box defines the domain of Figs. 2b and 16.

the duration of the warm sector that is the focus of this study.

Each rain trace (Fig. 7) indicates that relatively light stratiform rain ($\sim$1 mm h^{-1}) fell prior to the warm front, followed by a period of heavier rain ($\sim$10 mm h^{-1}) during the warm-frontal passage. Heavy rain also straddled the leading cold-frontal passage (i.e., NCFR), and a subsequent cessation in rainfall occurred prior to 0000 UTC 4 February. The primary difference in the character of these traces resides within the warm sector. Specifically, heavy rain persisted in the warm sector only at the westernmost gauge (LTP), whereas the warm-sector rainfall abated at the three eastern gauges. This lull increased from $\sim$5 to 7 h from west (BND) to east (EKN). WSR-88D radar observations from MUX confirmed the persistence of warm-sector rains only in the western Santa Cruz Mountains. Rainfall characteristics in the Santa Cruz Mountains during the warm-frontal passage and in the warm sector are discussed in more detail in section 5. The discussion here focuses on the crucial 6-h warm-sector period between 2200 UTC 2 February and 0400 UTC 3 February (gray shading in Figs. 7, 8) when synoptic forcing was weak (i.e., warm-frontal rain ended over the Santa Cruz Mountains at $\sim$2200 UTC and cold-frontal rain did not start until $\sim$0400 UTC).

Even though rainfall associated with the 2–3 February storm spanned 45 h, a very significant period, hydrologically, occurred in a narrower time window. The streamflow traces in Fig. 8 focus on this narrower window. Because heavy rains fell in the Santa Cruz Mountains the previous month (325–533 mm), it is reasonable to assume that the soil was saturated (or at least nearly so) and that a majority of the rainfall during this storm resulted in runoff. In these conditions, the streamflow behavior for a particular watershed depends primarily on the size of the watershed, the areal distribution of rainfall within it, and the time over which the rainfall occurs (Linsley et al. 1986). The four watersheds shown in Fig. 2b range in size from 72 to 275 km^2 (upstream of the stream gauges), so the streamflow response to rainfall should vary somewhat from one to the other. Nevertheless, the response time of these watersheds during this storm was similar, roughly 2–3 h (the term response time is used here to represent the time required for changes in rain rate over the watershed to be manifested by changes in streamflow at the stream gauge). The rain traces in Fig. 7 provided a reasonable estimate of basinwide rainfall in each of the four watersheds, as
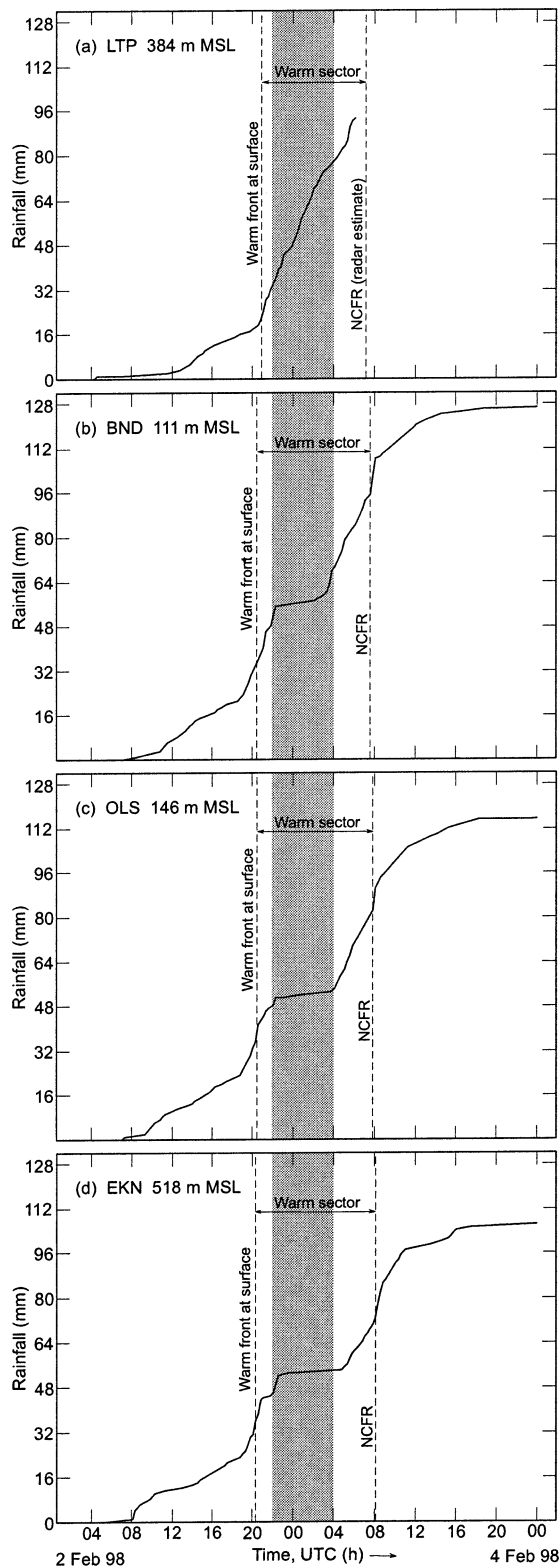
FIG. 7. Time series traces of accumulated rainfall (mm) at sites (a) LTP, (b) BND, (c) OLS, and (d) EKN as shown in Fig. 2b. The vertical dashed lines mark the passage of the warm front and narrow cold-frontal rainband (NCFR) at the surface at each site. The vertical gray-shaded bar identifies a crucial time period in the warm sector

determined by the MUX radar. Accordingly, these traces will be compared to corresponding streamflow data.

Streamflow in each watershed (Fig. 8) crested in response to the heavy cold-frontal rainfall (Fig. 7). The unique character of the observed warm-sector rainfall in the Pescadero Creek watershed (see LTP) relative to the three eastern watersheds is also reflected in the streamflow. Notably, Pescadero Creek rose steadily during the warm sector in response to the continuous warm-sector rainfall in the western Santa Cruz Mountains, whereas the streams to the east subsided during a crucial 4–6-h period in the warm sector in response to the lull in warm-sector rains there.

The measured traces in Fig. 8 are shown with traces that have been normalized with respect to the record flood observed in each watershed based on 45–50 yr of data. The normalized hydrographs show that the Pescadero flood peak was its record flood and that the peak followed the NCFR. The adjacent watershed at SLO, however, attained only ∼64% of its all-time record flow during the same post-NCFR period. The flood at SLO was only the fourth largest at this gauge. Hence, it is hypothesized here that the period when warm-sector rainfall abated within the highly populous San Lorenzo watershed (Fig. 7b) reduced the severity of its flood (Fig. 8b), whereas the persistence of warm-sector rains in the adjacent, but sparsely populated, Pescadero watershed (Fig. 7a) contributed substantially to its flood reaching record status (Fig. 8a). Farther east, the Soquel and Corralitos watersheds experienced peak post-NCFR flows that were even less significant (<40%) relative to their all-time records. The flood at these two gauges did not even rank in the top 10, quite likely because of the long lull in warm-sector rainfall in these watersheds (see section 5).

Stream gauge data from four runoff events on Pescadero Creek are used in appendix A to estimate what fraction of the record peak flow on Pescadero Creek at 0945 UTC 2 February was the result of runoff from rainfall that occurred during the warm-sector period from 2200 UTC 2 February to 0400 UTC 3 February. Although it was 5.75 h between the end of this period and the time of peak flow, ∼26 ± 9% of the peak flow was attributable to this 6-h period. Without the contribution of this runoff, the peak flow would have been between the third- and sixth-highest flood on Pescadero Creek.

5. The impact of coastal orography on rainfall distributions

Observations are now presented to demonstrate how the mesoscale distribution of warm-sector rainfall in the

←

between 2200 UTC 2 Feb and 0400 UTC 3 Feb. The rain gauge at LTP ceased operating at 0615 UTC 3 Feb when cold-frontal rain was falling.
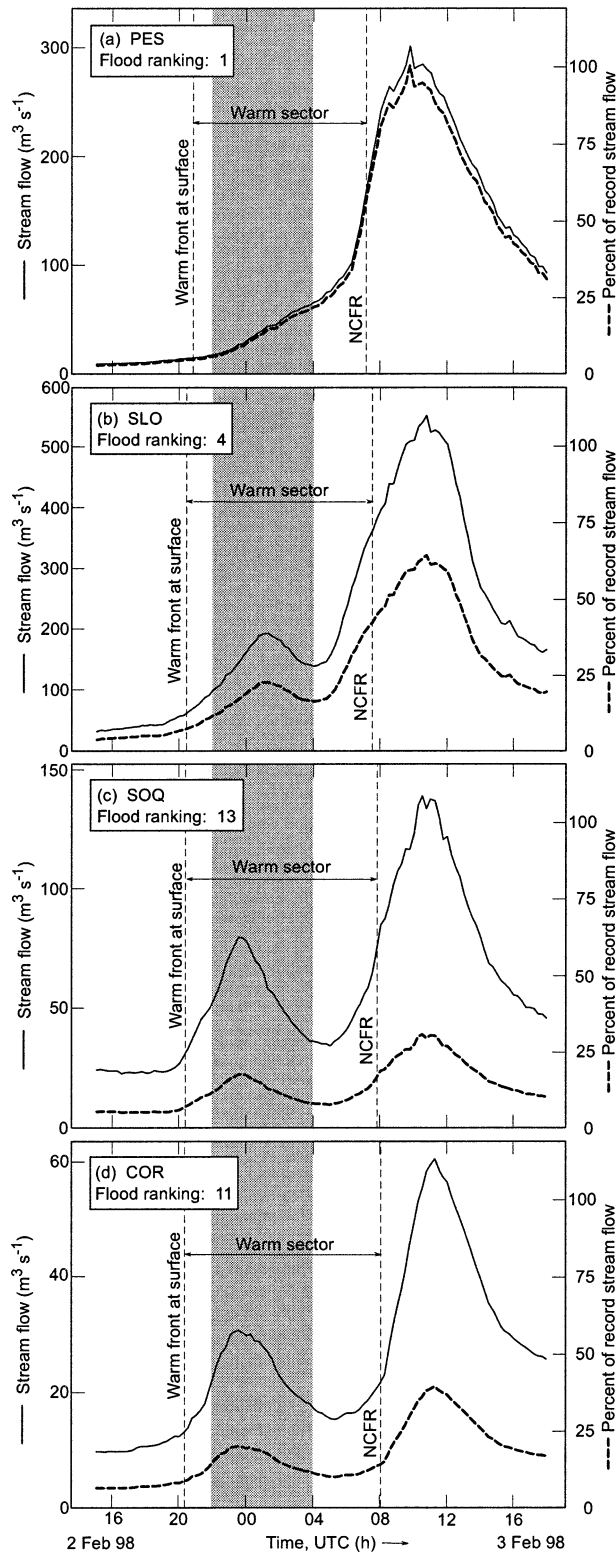
FIG. 8. Time series traces of measured streamflow (m³ s⁻¹; solid) and normalized streamflow (percent of record streamflow; dashed) at (a) PES, (b) SLO, (c) SOQ, and (d) COR. The normalized streamflow trace and peak-flow ranking at each site are based on a comparison with data dating back to 1950 at SLO and SOQ, 1952 at PES, and

Santa Cruz Mountains was modulated by the locally complex terrain. This includes documenting the orographic enhancement of precipitation on the windward slopes, the presence of a nearly perfect rain shadow in the lee of a coastal range, and the orientation of the lateral edge of this rain shadow relative to the key watersheds in the Santa Cruz Mountains.

a. Orographic rainfall enhancement in the cyclone warm sector

Wind-profiler and rain gauge data at PPB and rain gauge data at Three Peaks (TPK; Fig. 2a shows locations) help document the mesoscale features impacting the coastal zone on 2–3 February (Fig. 9). A time–height section of hourly wind profiles and upslope-component isotachs (Fig. 9a) shows the temporal descent of warm-frontal shear from ~4 km MSL at 1200 UTC 2 February to the surface 6 h later, followed by enhanced upslope flow in the warm sector. The surface passage of the leading cold front at 1000 UTC 3 February marked the end of the warm sector. The trailing cold front passed ~3 h later. Hourly wind profiles from the NPS profiler and the MUX radar (not shown) revealed very similar structures, albeit with slight timing differences. Light rain preceded the warm front, while the heaviest rain fell with the leading cold front (Figs. 9b,c). Frontal forcing likely contributed significantly to this rainfall, because the rain accompanied the fronts at both the coast (PPB, 11 m MSL) and in the downstream mountains (TPK, 1021 m MSL). In contrast, only the mountain site (TPK) recorded heavy rain with the surface warm-frontal passage and continuous rain in the warm sector. The ~6:1 ratio in warm-sector rainfall between TPK and PPB (only 22 km apart) highlights the orographic rain enhancement in the warm sector, and the lack of warm-sector rainfall at PPB indicates that the warm sector had weak synoptic forcing. Previous studies (e.g., Lowndes 1968; Browning et al. 1974; Hill and Browning 1979; Hill 1983) have shown that the heaviest orographic rains often occur within potentially unstable maritime warm sectors that do not contain significant large-scale lift, because the potential instability is preserved until acted upon by orographic lift. The P-3 data offshore revealed potential instability in the warm sector below ~4 km MSL in this case.

To quantify the impact of orographic forcing on rainfall within the warm sector of this storm, a correlation analysis was conducted between upslope flow at PPB and rain rate at TPK using the technique of Neiman et al. (2002). Based on their finding that the upslope layer near ~1 km MSL (i.e., near mountaintop) optimally controls orographic rainfall in California's coastal mountains, a

←

1955 at COR. These sites are shown in Fig. 2. The vertical dashed lines and gray-shaded bar are as in Fig. 7.
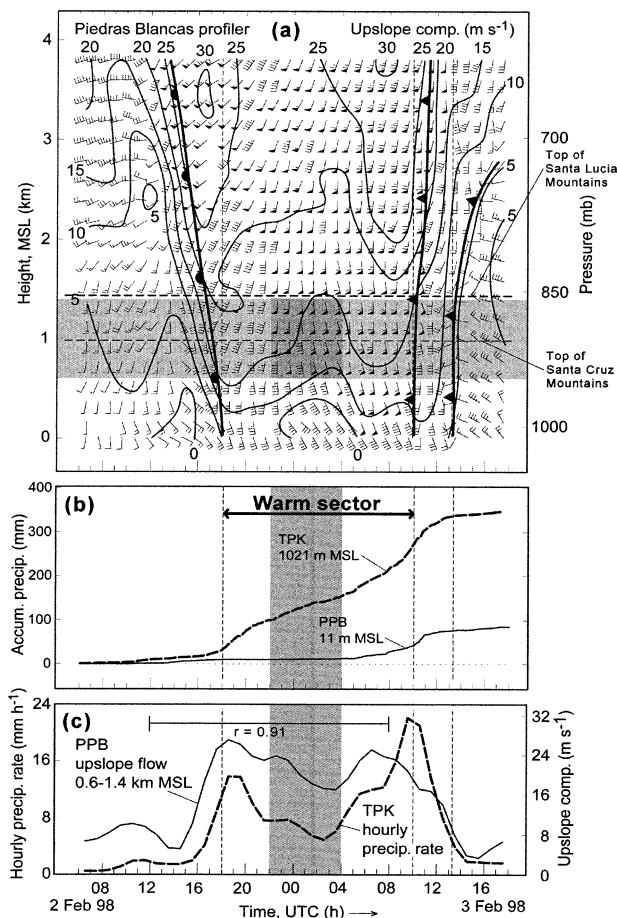
FIG. 9. (a) Time–height section of hourly averaged wind profiles, upslope-component isotachs (directed from 225°), and fronts at PPB (wind flags and barbs are as in Fig. 3). The wind-profiler data within the horizontal gray-shaded bar (0.6–1.4 km MSL) were layer-averaged and then presented in (c). (b) Time series of accumulated rainfall at PPB and TPK. (c) Time series of hourly-averaged, layer-mean upslope flow between 0.6 and 1.4 km MSL at PPB [layer shown in (a)] and corresponding hourly rain rate at TPK. The 20-h correlation coefficient between these two traces ($r = 0.91$) is shown. The vertical dashed lines in (b) and (c) mark the times of frontal passage at the surface; (a)–(c) the vertical gray-shaded bar is as in Fig. 7. Site locations are given in Fig. 2a.
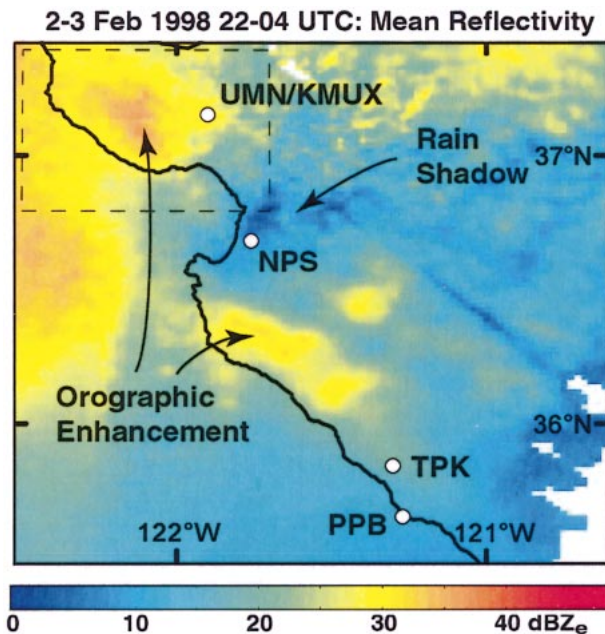

FIG. 10. The 6-h mean reflectivity (dBZ; see scale) based on the compositing of all 0.5°-tilt scans between 2200 UTC 2 Feb and 0400 UTC 3 Feb 1998 from the WSR-88D radar at MUX. The PPB and NPS wind-profiler sites and TPK and UMN rain gauge sites are also shown. The dashed inset box defines the domain of Figs. 2b and 13.

linear correlation analysis was carried out using layer-mean profiler wind measurements between 0.6 and 1.4 km MSL that straddled the top of the Santa Cruz Mountains and lay just beneath the top of the Santa Lucia Mountains (see Fig. 9a). The time window used in the correlation analysis (Fig. 9c) ends with the leading cold front, where frontal forcing dominated. A strong correlation of 0.91 was present in the warm sector. As a result, 83% of the hour-to-hour variability in warm-sector rain rate at TPK is attributed to linear changes in the upslope component of the flow impacting the coastal mountains. Because the same synoptic conditions existed over the Santa Cruz Mountains, and the persistence of warm-sector rainfall at LTP was similar to that at TPK, it is concluded that the warm-sector rain that fell on the Pescadero

Creek watershed was also primarily orographically forced.

A plan-view of the rainfall within the core of the warm sector over the coastal mountains is provided in the 6-h mean reflectivity derived from the WSR-88D radar at MUX ending at 0400 UTC 3 February (Fig. 10). This 6-h time window corresponds to the crucial period when the warm-sector rainfall abated in the central and eastern Santa Cruz Mountains. Orographic rainfall enhancement was clearly observed by the radar over the Santa Lucia and western Santa Cruz Mountains, although the heavy rainfall at TPK was not well sampled because the lowest scan mostly overshot the rather shallow echoes at this extended range (>100 km). Distinct rain shadowing was present downstream (north) of the Santa Lucia Mountains over NPS and in the eastern Santa Cruz Mountains. Echoes offshore marked the heavy cold-frontal rains approaching the coast at the end of the averaging period. The possibility that a nonorographically forced rainband stalled over the western Santa Cruz Mountains and contributed to the heavy rain was ruled out based on detailed examination of rain gauge and WSR-88D data. The fortuitous proximity of the MUX radar to the orographic rainfall enhancement in the western Santa Cruz Mountains (~23 km) provided quantitative precipitation estimates (QPE; presented later) without brightband contamination at the low altitudes sampled.
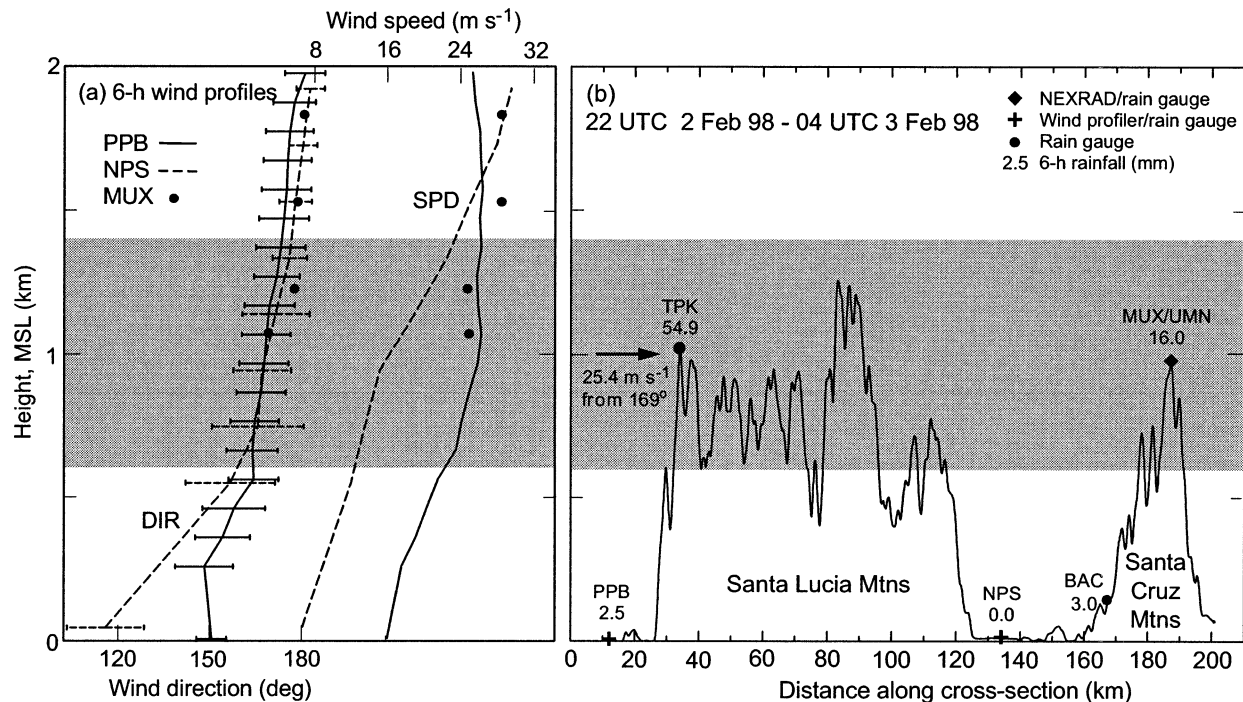
FIG. 11. (a) The 6-h mean profiles of wind direction (with std dev bars) and speed between 2200 UTC 2 Feb and 0400 UTC 3 Feb 1998 from PPB, NPS, and MUX (see key). (b) Cross section of terrain along AA' in Fig. 2a. The 6-h rainfall totals at PPB, TPK, NPS, BAC, and UMN are shown. The bold arrow and velocity information in (b) is the 6-h layer-mean wind velocity measured by the PPB wind profiler between 0.6 and 1.4 km MSL (gray-shaded bar).

b. The Santa Lucia rain shadow

During the 6-h period when orographically forced warm-sector rainfall in the Santa Cruz Mountains was observed primarily along its western flank (Figs. 7, 10), the layer-mean wind in the 800-m-deep layer at PPB that controlled the orographic forcing (dark-shaded rectangle in Fig. 9a) was 25.4 m s^{-1} from 169° with a standard deviation in wind direction of 8°. The orographic rainfall maximum was situated west of a flow-parallel line that emanated from the northwestern tip of the Santa Lucia Mountains (Fig. 2a); this north-northwestward-pointing line represents the regionwide mountaintop flow orientation since the 6-h-averaged wind-direction profiles from PPB, NPS, and MUX within the 800-m-deep controlling layer were nearly identical (Fig. 11a). To the west of this line, moist low-level air directly ascended the Santa Cruz Mountains from the open ocean during this 6-h period. As a result, extreme orographic enhancement of rainfall occurred over the western flank of the Santa Cruz Mountains (Fig. 12a) between the coastal rain gauge at DAP (3 m MSL) and the mountain gauge at LTP (384 m MSL), similar to that observed at the TPK–PPB couplet (Fig. 9b). The lack of rainfall at DAP highlights the weak synoptic forcing over the region during this period. To the east of this line, the low-level flow initially encountered the Santa Lucia Mountains, causing heavy orographic rains there, before descending the steep lee side where a rain shadow ex-

tended downstream over the central and eastern Santa Cruz Mountains (Figs. 10, 11b). Figure 11b shows a 20-fold orographic enhancement in 6-h rainfall between the coast and the initial crest of the Santa Lucias at TPK, and a profound rain shadow downstream of the Santa Lucias at NPS, where no rain fell during this period. Because of rainout over the Santa Lucia range, the downstream mountain site at UMN (942 m MSL) received only 16 mm of rain in 6 h, or just 29% of that observed at TPK at a comparable altitude (Fig. 11b). Similarly, the orographic rainfall enhancement in the dessicated airstream ascending the eastern Santa Cruz Mountains between BAC and UMN (Fig. 12b) was less than that in the airstream impacting the western Santa Cruz Mountains (Fig. 12a). Because the airstreams on either side of this line possessed fundamentally different histories, this line represents a dividing streamline originating from the westernmost portion of the Santa Lucias.

Although the rain gauges in the Santa Cruz Mountains provided valuable quantitative information highlighting the influence of the dividing streamline on the 6-h warm-sector rainfall distribution, the spacing of these gauges was too coarse to capture the orographic rainfall maximum observed in the western Santa Cruz Mountains by the fortuitously positioned WSR-88D S-band radar at MUX (Fig. 10). To fill this critical observational gap in rain gauge data, an appropriate reflectivity–rain-rate
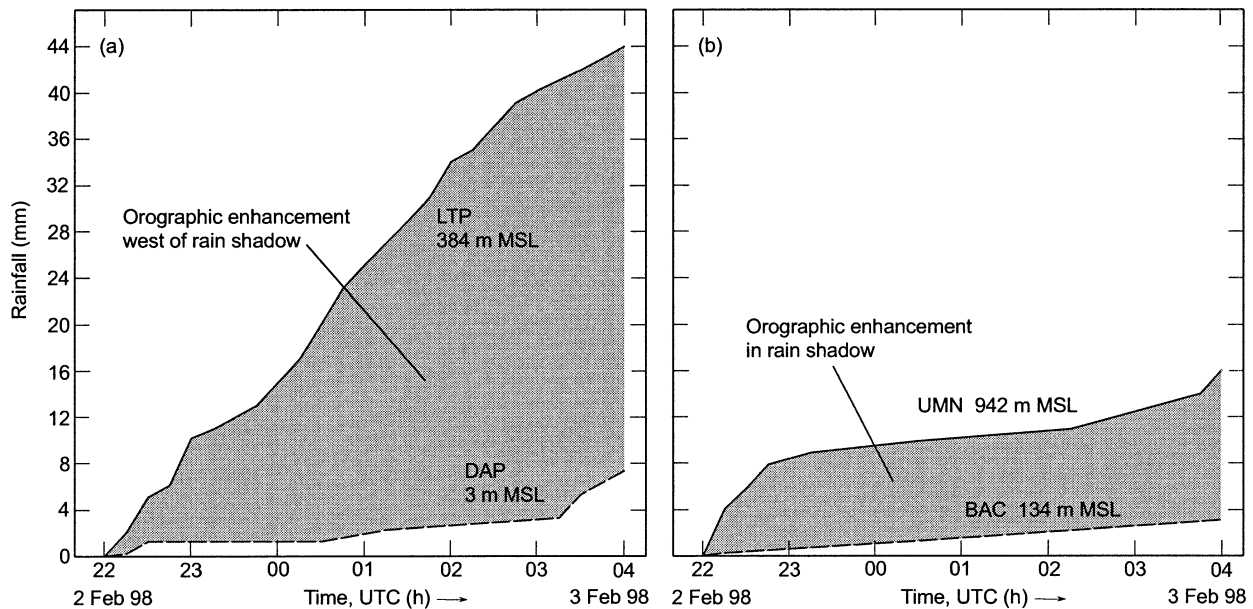
FIG. 12. Time series traces of accumulated rainfall (mm) at (a) LTP and DAP, west of the Santa Lucia rain shadow; and (b) UMN and BAC, within the Santa Lucia rain shadow. These sites are shown in Fig. 2. Shading denotes the orographic rainfall enhancement between the coastal and mountain sites.

(Z–R) relationship was applied to the 6-h mean radar reflectivity analysis within the inset box of Fig. 10. The Z–R relationship used [$Z = 118R^{1.5}$, where Z is reflectivity (mm^6 m^{-3}) and R is rain rate (mm h^{-1})] was derived from the analysis of experimental, vertically pointing, S-band radar data and collocated rain gauge data collected in the coastal mountains northwest of San Francisco during this same storm (not shown). It was assumed that the coastal mountain rainfall near MUX possessed similar microphysical attributes.[3] The resulting 6-h QPE (Fig. 13a) show heavy orographic rainfall (30–48 mm) localized over the western half of the San Lorenzo watershed to the west of the dividing streamline. Rainfall was much lighter to the east of this streamline, including over the highest portion of the Santa Cruz Mountains, within the rain shadow. Because the populous San Lorenzo watershed is contained in a 20° wedge whose apex originated from the westernmost portion of the Santa Lucia Mountains, a ±10° variation in wind direction (which is greater than the observed 6-h layer-mean standard deviation in wind direction of 8°) would have placed the heavy orographic rains completely in or out of this populous watershed.

It is reasonable to assume that the 6-h period of light rainfall east of the dividing streamline (see Fig. 13a) accounted for the ~6-h decrease in streamflow observed at the SOQ and COR stream gauges (Figs. 8c,d). How-

ever, west of the dividing streamline (Fig. 13a) the 6-h QPE showed heavy rain primarily in the San Lorenzo watershed, even though the streamflow subsided for 3 h at SLO and increased steadily at PES within this 6-h period (Figs. 8a,b). This discrepancy suggests that the position of the radar-estimated rainfall maximum was situated too far south. To address this inconsistency, a comparison was made between the QPE field and the rain gauge data in the area. Correlation and rms error analyses based on spatial shifts of the QPE pattern relative to the ground (appendix B) revealed a roughly 7.5-km southward offset of the QPE field, given the underestimate of rainfall north of the QPE maximum and the overestimate to the south. This offset would result from northward advection of hydrometeors as they fell through the strong southerly flow between the altitude of the radar beam and the ground. Measurements of the horizontal wind speed in the key layer between 0.6 and 1.4 km MSL (Fig. 11a), combined with inferred hydrometeor fall speeds and vertical air motions, indicate that such an offset is realistic in its magnitude (appendix B). The corrected position of the QPE rainfall maximum placed it within the Pescadero Creek watershed (Fig. 13b) where the record flooding occurred. In short, the strong low-level southerly flow forced the rainfall maximum to occur on the lee side of the east–west-oriented ridge separating these two watersheds. This QPE result illustrates the importance of downstream drift of hydrometeors when assessing the possibility of flooding in adjacent watersheds in the LLJ. Incorporating the advection of hydrometeors into NWS's new Flash Flood Mapping Program could prove critical to operations

---

[3] The experimental Z–R relationship provided a closer estimate of the areawide rainfall in the vicinity of the Santa Cruz Mountains than did the default WSR-88D Z–R relationship [$Z = 300R^{1.4}$; Fulton et al. (1998)], which significantly underestimated the rainfall (see appendix B).
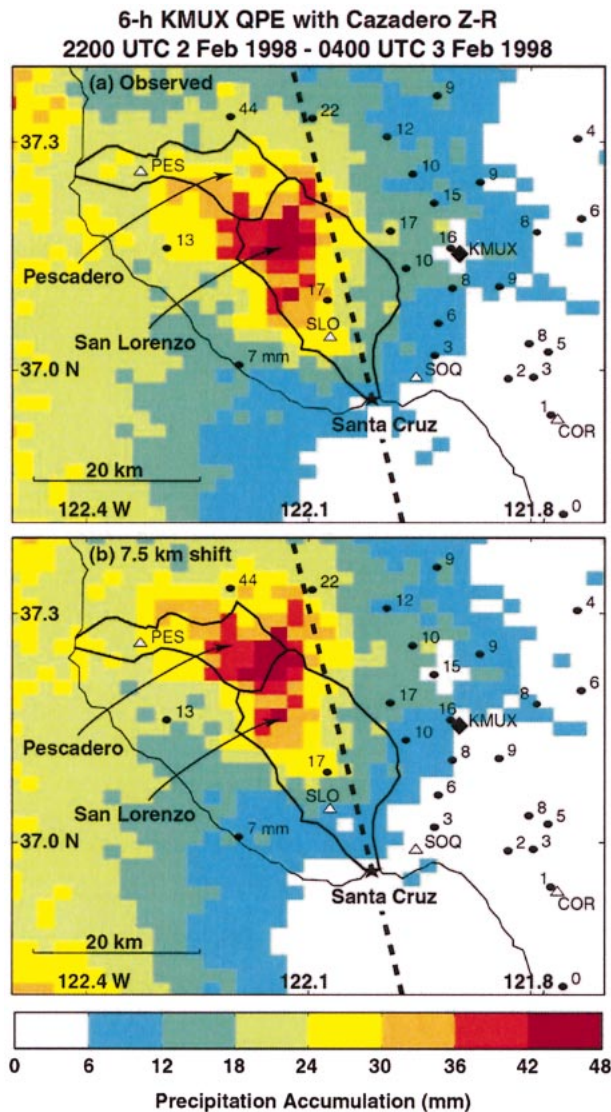
FIG. 13. (a) Quantitative precipitation estimate QPE (mm, see scale) for the 6-h period 2200 UTC 2 Feb to 0400 UTC 3 Feb 1998 based on a coastal mountain *Z–R* relationship applied to the mean reflectivity field shown in Fig. 12. (b) As in (a) but for the QPE field advected 7.5 km downstream from 169°. (a), (b) 6-h rainfall totals (rounded to the nearest mm) are next to the corresponding rain gauge sites (bold dots). The four stream gauges labeled in Fig. 2b are also shown here (open triangles). The Pescadero and San Lorenzo watersheds are outlined. The bold dashed line marks the dividing streamline from 169° (see also Fig. 2a).

(i.e., the existing algorithm would have placed the maximum rainfall in the wrong watershed).

These observations show that heavy orographic warm-sector rain fell in the Santa Cruz Mountains to the west of the 169° dividing streamline during the key 6-h period, and that this rain contributed significantly to the flood reaching record status in Pescadero Creek (see appendix A). Earlier, however, a ~2 h burst of heavy rainfall occurred to the east of this streamline, starting ~1 h before the surface passage of the warm
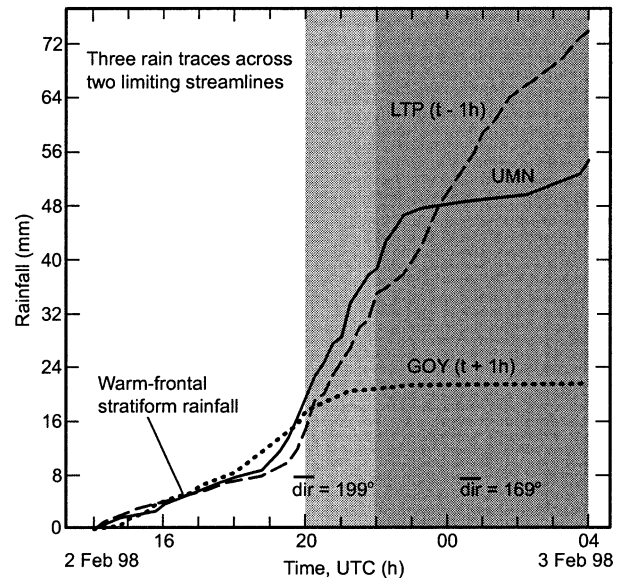

FIG. 14. Time series traces of accumulated rainfall (mm) at LTP, UMN, and GOY (sites shown in Fig. 2a). The traces at GOY, UMN, and LTP begin at 1300, 1400, and 1500 UTC 3 Feb 1998, respectively. The time coordinate is shifted for GOY and LTP to line up the warm-frontal passage. The dark-shaded bar identifies the crucial time period between 2200 UTC 2 Feb and 0400 UTC 3 Feb 1998, and the light-shaded bar denotes the 2-h period that straddles the warm-frontal passage at the surface. The time-averaged wind direction in the layer between 0.6 and 1.4 km MSL is shown for each gray-shaded time window.

front (Figs. 7b–d). The wind-profiler and rain gauge analyses in Fig. 9 demonstrate the orographic character of the heavy rain during the warm-frontal passage, and also show the onset of this 2-h burst preceding the warm-frontal passage at the surface. The 2-h burst commenced when enhanced upslope flow associated with a moist, but short-lived, southwesterly airstream on the warm side of the warm front descended through the 800-m-deep controlling layer (Fig. 9a). Analyses of hourly wind profiles from NPS and MUX (not shown) also showed this descending tongue of enhanced southwesterly component upslope flow. Because of the orographic nature of the forcing during this period, the impact of the Santa Lucia rain shadow on the rainfall distribution was considered. The ~2-h period of enhanced southwesterly component flow observed in the controlling layer on the warm side of the warm front at PPB, NPS, and MUX yielded a dividing streamline of 199° directed from the northwestern tip of the Santa Lucias (Fig. 2a).

The impact of both dividing streamlines on the rainfall coverage is shown in Fig. 14. During the brief period of southwesterly flow that followed the warm-frontal passage in the controlling layer aloft, sites west of the 199° dividing streamline (e.g., UMN) received a burst of heavy rainfall when moist warm-sector air ascended the Santa Cruz Mountains directly from the open ocean. In contrast, sites east of the 199° dividing streamline

(e.g., GOY) did not receive this burst because the warm-sector airstream resided in the Santa Lucia rain shadow. Later, heavy warm-sector rainfall abated during the 6-h period to the east of the 169° dividing streamline within the rain shadow (e.g., UMN) but continued to the west of this streamline (e.g., LTP). The briefly heavy warm-frontal rain and subsequent westward shift of the dividing streamline accounted for the secondary peak in streamflow shown in Figs. 8b–d. If the immediate post-warm-frontal flow in the controlling layer had not rotated from 199° to 169°, these watersheds and the city of Santa Cruz would have received significant additional rainfall and would have been at a heightened risk of catastrophic flooding.

6. Climatological perspective on flooding in adjacent watersheds

The earlier analysis highlights the sensitivity of flooding in adjacent coastal mountain watersheds to the low-level wind direction in a well-observed case study. This section explores how this is manifested in the long-term records of flooding in these watersheds, including the influence of short-term climate-scale variability associated with the El Niño–Southern Oscillation (ENSO). This is accomplished by using a roughly 50-yr history of streamflow data, global gridded tropospheric analyses, and the multivariate ENSO index (MEI; Wolter and Timlin 1993, 1998).

Many studies have investigated the connection between ENSO and California weather, including the impact of ENSO on precipitation (e.g., Schonher and Nicholson 1989; Livezey et al. 1997; Dettinger et al. 1998; Cayan et al. 1999) and streamflow (e.g., Kahya and Dracup 1994; Cayan et al. 1999; Andrews et al. 2004). These studies show a south-to-north decrease in anomalous winter-season rainfall and flooding during the warm or El Niño phase, and an opposite trend during the cold or La Niña phase. These trends are tied to the large-scale weather patterns over the eastern Pacific. For example, the subtropical and polar jet streams are often displaced southward and eastward during El Niño conditions (e.g., Rasmusson 1985; Cayan and Webb 1992; Livezey et al. 1997), resulting in an anomalous southern storm track that most heavily impacts southern California.

The following discussion relating flooding in adjacent watersheds to climate-scale variability is based on an analysis of streamflow data first presented in Andrews et al. (2004). They determined the magnitude and date of the annual peak flood (defined as the largest yearly streamflow episode at each site) for each of ~50 yr at each of 38 stream gauges in California's coastal mountains.[4] Then, for each annual peak flood at each site,

[4] Coastal mountain streamflow data were used, because rainfall is more sensitive to ENSO in California's coastal mountains than in the interior highlands (Schonher and Nicholson 1989).
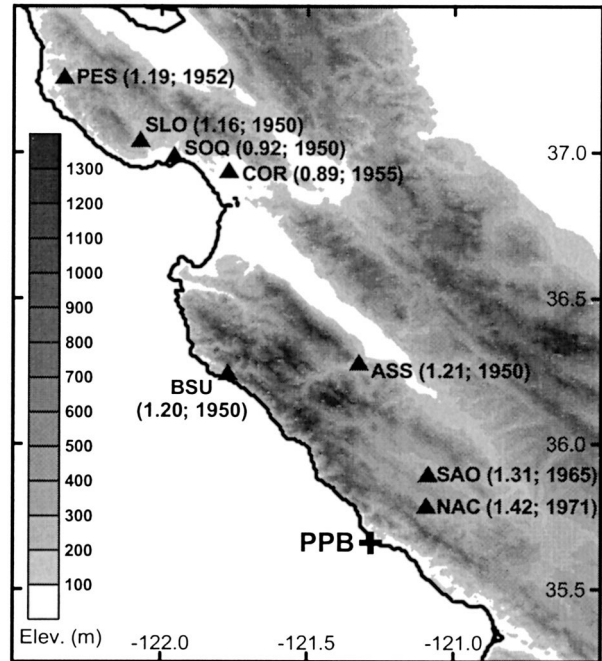

FIG. 15. Terrain base map showing the locations of the stream gauge stations (▲) in CA central-coast region. The normalized El Niño flood magnitude for a 5-yr flood, based on recorded annual peak flows for El Niño and non–El Niño conditions, is shown in parentheses next to each station name. The second number in each pair of parentheses is the year that data were initially recorded at that site; all sites gathered data through 2000. The wind-profiler site at PPB is shown.

they categorized the concurrent MEI as either El Niño (MEI ≥ 0.5) or non–El Niño (MEI < 0.5). Finally, they calculated a ratio at each site referred to as the normalized El Niño flood magnitude or R_q. This ratio is based on the relative magnitudes of the El Niño and non–El Niño annual peak floods with an exceedence probability of 0.20 (i.e., floods with an average 5-yr return interval) at each site (Q_{el} and Q_n, respectively). The value R_q ranges from 2 when El Niño flooding dominates to 0 when non–El Niño flooding dominates, and equals 1 when flooding in these two ENSO regimes are the same magnitude. The value R_q decreased from nearly 2 in the south to only ~0.8 in the north, thus revealing that flood events whose discharges equaled the magnitude of a 5-yr flood were tied to El Niño and non–El Niño conditions in coastal southern and northern California, respectively. Their linear regression fit for R_q versus latitude yielded a correlation coefficient of 0.95, that is, latitude explained 90% of the south-to-north variation in the normalized El Niño flood magnitude across coastal California. Two outlying data points were excluded from this correlation analysis: Soquel (SOQ) and Corralitos (COR) in the eastern Santa Cruz Mountains.

Figure 15 shows the general south-to-north decrease in R_q across the central California coast, except for the

outliers at SOQ and COR. These sites were the only two south of ~39.5° latitude where the magnitude of the 5-yr El Niño flood was less than the 5-yr non–El Niño flood. As shown in the following, these outliers provide the link between climate-scale variability associated with ENSO and orographically generated flooding in the Santa Cruz Mountains. This link is established using composite analyses from daily global gridded data from the National Centers for Environmental Prediction–National Center for Atmospheric Research (NCEP–NCAR) reanalysis project (e.g., Kalnay et al. 1996). Composites were created for El Niño conditions (MEI $\geq$ 0.5) and for non–El Niño conditions (MEI < 0.5). For each annual peak flood at each of the stream gauges in Fig. 15, the daily gridded data for the day of the flood and the day preceding the flood were included in the composites. If more than one stream gauge measured an annual peak flood on the same date, the corresponding gridded data were included in the appropriate composite only once. A total of 86 and 194 daily gridded analyses were used in the El Niño and non–El Niño composites, respectively.

To characterize the difference in the mean direction of the low-level flow impacting the coastal mountains during the El Niño and non–El Niño annual peak floods, 925-mb geopotential height (i.e., geostrophic flow) composites were constructed (Figs. 16a,b). Before discussing these composites, however, it is important to recognize that the 925-mb geostrophic wind direction can differ from the actual wind direction along the California coast during landfalling storms due to ageostrophic processes such as surface friction and blocking by coastal mountains. For example, a mesoscale ageostrophic barrier jet often develops in response to the blocking of low-level flow upstream of quasi-two-dimensional mountain ranges (e.g., Parish 1982; Marwitz 1987; Overland and Bond 1995; Doyle 1997; Yu and Smull 2000). Thus, the observed low-level flow during landfalling storms is typically rotated counterclockwise relative to the geostrophic flow, as the following comparison reveals. The mean wind direction at ~925 mb recorded by the PPB wind profiler during all major rain events from the El Niño winter of 1997/98 was 203°, whereas the composite 925-mb geostrophic flow for these same events was from 227°. Because this 24° offset is a result of ageostrophic processes (e.g., blocking and surface friction) that are present independent of ENSO's phase, to a first order this offset is assumed to apply to other years used in the composites.

The 925-mb geopotential height composite for El Niño years (Fig. 16a) yielded a geostrophic wind direction of 227° over the Santa Cruz Mountains, identical to the composite flow based on the rain events from the El Niño winter of 1997/98. In contrast, the non–El Niño composite (Fig. 16b) resulted in a geostrophic flow from 241°. This difference is consistent with the observation that storm circulations during developed El Niño episodes tend to be more meridional than those during non–

El El Niño episodes (e.g., Rasmusson and Wallace 1983; Webb and Betancourt 1992). Assuming the observed flow was rotated counterclockwise by 24° relative to the geostrophic flow (see previous paragraph), this compositing result provides an explanation for the gradient of R_q between PES and COR, and for the anomalous response of flooding at SOQ and COR to the ENSO state. Namely, the mean low-level meridional flow that accompanies storms during El Niño impacts the SOQ and COR watersheds only after moisture in this airstream has been depleted by orographic ascent over the Santa Lucia Mountains, whereas the more zonal low-level flow that accompanies storms during non–El Niño conditions results in a direct fetch from the ocean into these watersheds. Hence, the eastern Santa Cruz Mountains have peak streamflows that are anomalously low due to rain shadowing during El Niño years (MEI $\geq$ 0.5) and anomalously high during non–El Niño years (MEI < 0.5).

The PES and SLO watersheds in the western Santa Cruz Mountains experience unobstructed onshore flow in both ENSO regimes. However, the 925-mb composite geostrophic wind speed is 20% greater during El Niño conditions (Figs. 16a,b), resulting in stronger orographic forcing of rainfall (Neiman et al. 2002). Additionally, the 925-mb composite temperature and mixing ratio are 0.3°C and 0.2 g kg^{-1} greater during El Niño conditions, and the 1000–700-mb lapse rate is 0.4°C steeper. Though the magnitude of these thermodynamic differences is not large, Persson et al. (1999) showed that similar low-level enhancements observed during the landfall of this storm in southern California resulted in a 26% increase in convective available potential energy. Therefore, the El Niño phase of ENSO is characterized by large-scale conditions that are more favorable for orographic rainfall enhancement, consistent with the long-term streamflow observations that favor flooding at PES and SLO during El Niño episodes. These results suggest that the ENSO-dependent large-scale thermodynamic and wind speed conditions at low levels play a primary role in modulating flooding at PES and SLO, whereas the ENSO-dependent low-level wind direction (and, therefore, the position of the dividing streamline) is primarily responsible for modulating flooding at SOQ and COR.

Having linked ENSO to annual peak flooding in four adjacent watersheds of the Santa Cruz Mountains, additional composite analyses are presented to determine the low-level flow associated with the largest floods in these watersheds. Using the same compositing technique as previously, an additional composite pair was created to characterize the mean difference in 925-mb flow impacting the PES and COR watersheds during all flooding events surpassing the 5-yr flood threshold (a total of 12 and 7 floods, respectively). The composite geostrophic wind direction associated with the largest floods at PES (225°; Fig. 16c) was very similar to that observed during El Niño conditions (227°; Fig. 16a),
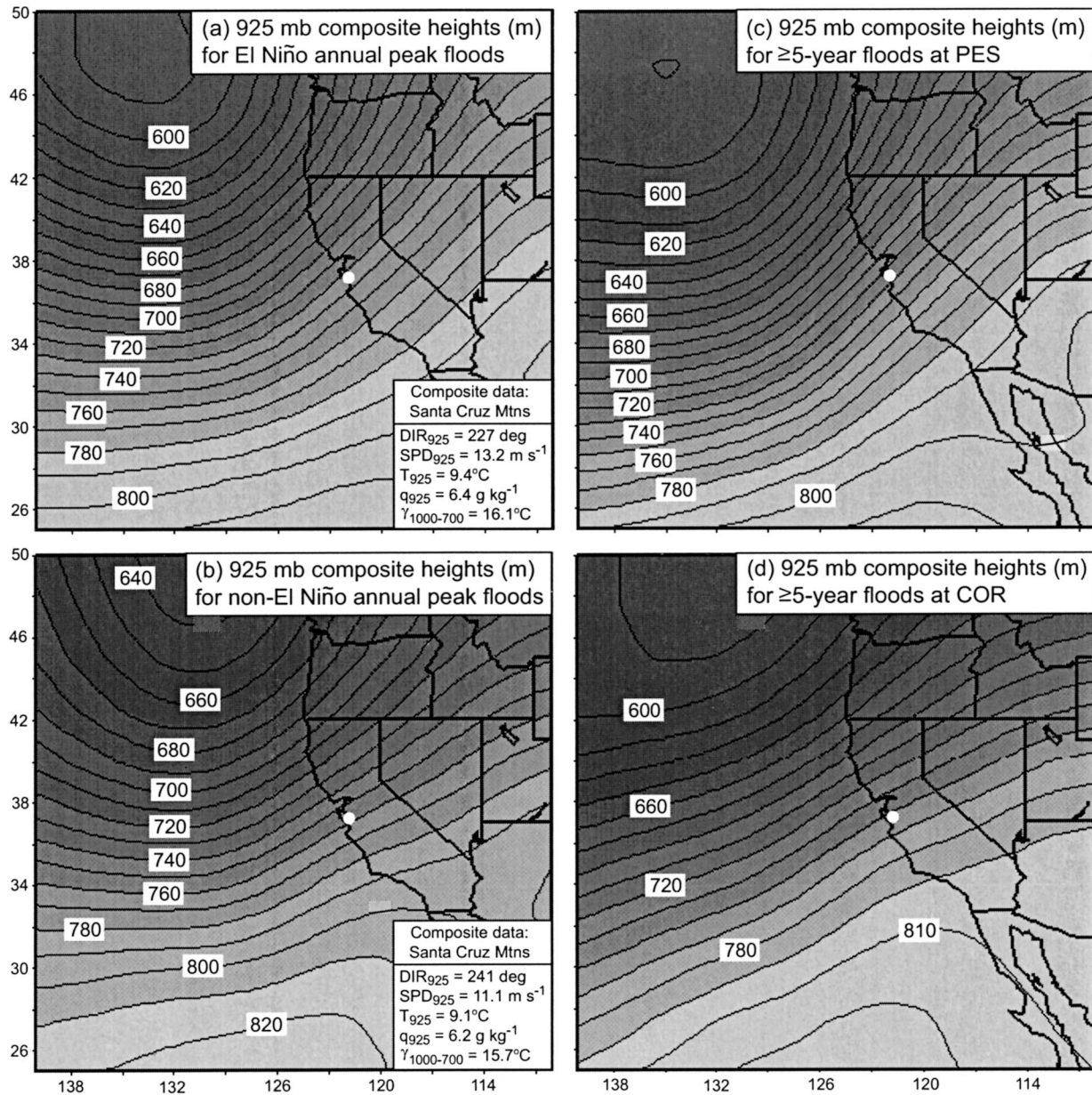
FIG. 16. Composite 925-mb geopotential height fields (m) based on the NCEP–NCAR reanalysis global gridded dataset during: (a), (b) the annual peak flood at each of the eight stations in Fig. 15 for El Niño and non–El Niño conditions; and (c), (d) during all streamflow events surpassing the 5-yr flood threshold at PES and COR. (a)–(d) The white dot marks the location of the Santa Cruz Mountains. (a), (b) The tables contain composite data at 925 mb (DIR$_{925}$ = geostrophic wind direction, SPD$_{925}$ = geostrophic wind speed, T_{925} = temperature, q_{925} = mixing ratio), and composite lapse-rate data between 1000 and 700 mb ($\gamma_{1000-700}$), for the Santa Cruz Mountains. Lat and lon labels at left and bottom.

and the composite direction accompanying the largest floods at COR (242°; Fig. 16d) mirrored the non–El Niño value (241°; Fig. 16b). These results further highlight the sensitivity of long-term flooding characteristics in adjacent watersheds to the direction of the low-level flow.

It should be noted that the NCEP–NCAR reanalyses can miss potentially important mesoscale details (e.g.,

LLJs, frontal circulations, convection). However, the composites of these reanalyses are generally consistent with the case study results, thus suggesting that the composites have captured critical elements of the conditions modulating peak streamflows in the Santa Cruz Mountains. Long-term wind-profiler observations in this area, hopefully lasting several ENSO cycles, have been initiated to observe the variation of the ENSO-dependent
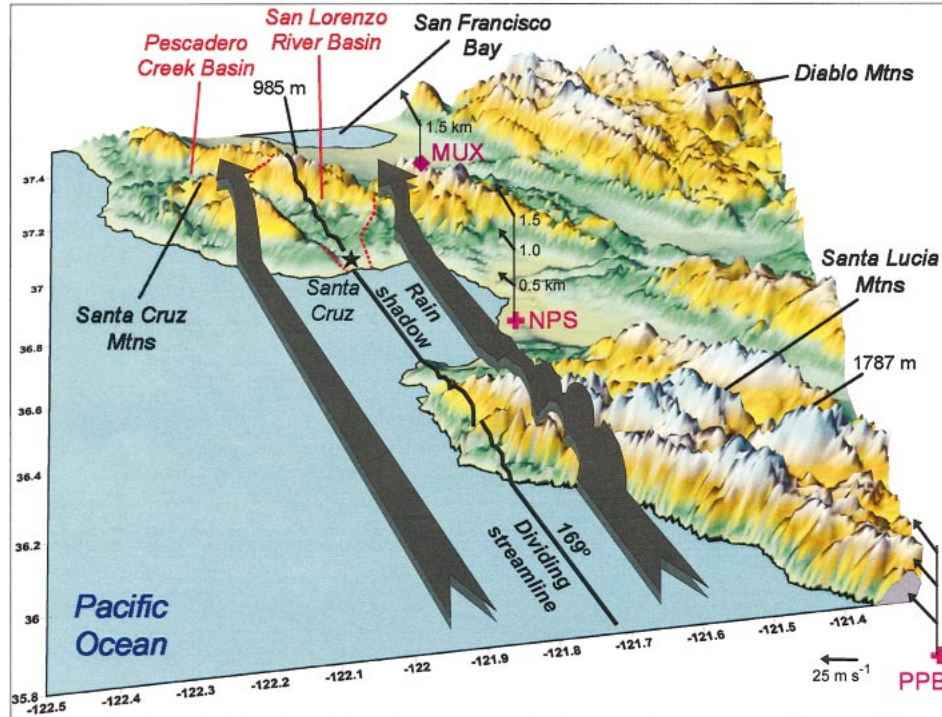
FIG. 17. Conceptual representation of the dividing streamline separating a moist low-level airstream that directly ascended the western Santa Cruz Mountains from the open ocean and a desiccated low-level airstream within the Santa Lucia rain shadow that ascended the eastern Santa Cruz Mountains. The locations of the WSR-88D radar at MUX and the wind profilers at NPS and PPB are shown, as are scaled 6-h-averaged wind vectors between 2200 UTC 2 Feb and 0400 UTC 3 Feb 1998 from these sites. The red dashed lines enclose the San Lorenzo watershed.

low-level wind characteristics and their impacts on peak streamflow.

7. Conclusions

Analyses of experimental and operational data collected during the major landfalling storm of 2–3 February 1998 during the California Land-falling Jets Experiment (CALJET; Ralph et al. 1999) are used to describe the role of orographic processes in modulating flooding in the Santa Cruz Mountains on the California coast. Significant differences in the magnitude of flooding on adjacent watersheds were attributed to the influence of a rain shadow that occurred during a 6-h period within the warm sector of the storm. This period was characterized by highly efficient orographic rainfall enhancement on windward slopes [as documented using NOAA/ETL's experimental wind-profiler array and techniques developed by Neiman et al. (2002) that identified a controlling layer at ~1 km MSL for orographic rain] and by a prominent rain shadow on the lee side of the Santa Lucia Mountains. The rain shadow was especially well defined in rain gauge and WSR-88D radar data, similar to that observed in an eastern U.S. storm by Brady and Waldstreicher (2001).

The combination of the local terrain orientation and the roughly southerly flow direction in the controlling layer created a dividing streamline marking the lateral (western) boundary of the rain shadow cast by the Santa Lucia Mountains upon the Santa Cruz Mountains (Fig. 17) during the key 6-h period within the warm sector. East of where this streamline crossed the Santa Cruz Mountains, a 4–6-h cessation of rainfall was observed, and flooding was less severe than to its west. West of this line, in the Pescadero Creek watershed, rainfall continued throughout this key period. Based on multiple wind-profiler observations of wind direction, which agreed to within ±1°, and on rain gauge and WSR-88D radar data, it was found that the dividing streamline bisected the next watershed to its east, which is the heavily populated San Lorenzo Creek watershed. If the wind direction controlling the orientation of the dividing streamline was rotated clockwise by only a few degrees, the San Lorenzo Creek watershed and the city of Santa Cruz would have received significantly more rain, thus increasing the risk of catastrophic flooding. Conversely, a counterclockwise rotation of a few degrees would have lessened the Pescadero Creek flood. Without the rainfall from this 6-h period, the peak flow on Pescadero Creek would have been 26 ± 9% lower than it was (i.e., third- to sixth-highest flood rather than first).

The conclusions of the detailed case study were used

to explore the connection between local flooding variability and larger-scale conditions influenced by ENSO. Specifically, 50 yr of streamflow data from California's coastal mountains were examined to select key flood events for inclusion in composite analyses of 925-mb height patterns from the NCEP–NCAR reanalysis data. This approach confirmed that prominent case study evidence for wind–rainfall relationships and variable flow-dependent impact of the rain shadow cast across the Santa Cruz Mountains by the upstream (more southern) Santa Lucia range on 2–3 February are also expressed in the climatological record over multiple ENSO periods. The phase of ENSO impacted the probability of flooding quite differently on the western and eastern sides of the windward slope of the Santa Cruz Mountains. The western watersheds were found to have their greatest floods during El Niño events (MEI > 0.5), while the eastern watersheds peaked during non–El Niño episodes (MEI < 0.5). These results are consistent with the case study in that the composite 925 mb, meridionally oriented wind direction during El Niños favors a rain shadow over the eastern watersheds. During non–El Niño periods, the composite wind direction is more zonal such that the sheltering effect of the Santa Lucia rain shadow on the eastern watersheds of the Santa Cruz Mountains is greatly reduced, whereas weaker winds, less water vapor, and stronger stratification reduce the peak runoff in the western watersheds.

This study explored the mechanisms responsible for modulating, on the scale of key coastal watersheds, the precipitation and runoff in landfalling West Coast storms, and illustrated the connection between weather and short-term climate variations by describing how these mechanisms are modulated by ENSO. This was accomplished through the use of data gathered during CALJET, which documented a flood of record near Santa Cruz in February 1998, and through examination of the correlation between flooding and ENSO over several decades. Although motivated by a serious regional problem, the results presented here have bearing on many areas around the globe, and shed light on processes that lead to highly local variations in the relationship between the phase of ENSO and the occurrence of extreme floods on individual watersheds. Significant future work remains to explore this behavior in other regions and to assess the predictability relative to the need to forecast wind direction as accurately as ±10° (this study), or even as precisely as ±1° (Nuss and Miller 2001).

APPENDIX A

The Contribution of Warm-Sector and Warm-Frontal Rainfall to the Flood Peak During Pescadero Creek's Record Flood on 3 February 1998

The analysis presented in this appendix explores how much of the record flow in Pescadero Creek at 0945 UTC 3 February 1998 was a result of rain that fell: (a) during a key 6-h period of orographic forcing (i.e., between 2200 UTC 2 February and 0400 UTC 3 February) within the warm sector of the storm when the adjacent San Lorenzo watershed was partially within the rain shadow created by the Santa Lucia Mountains as described in section 5, and (b) during the warm-frontal period of the storm (ending at 2200 UTC 2 February).[A1] This analysis is conducted under the assumption that the total time-dependent runoff [$S_{tot}(t)$] is the sum of contributions of streamflow attributable to rainfall during the warm-frontal period [$S_{wf}(t)$], during the non-rain-shadowed, orographically forced warm sector [$S_{ws}(t)$], and during the pre-cold-frontal and cold-frontal rainbands after 0400 UTC 3 February [$S_{cf}(t)$]:

$$S_{tot}(t) = S_{wf}(t) + S_{ws}(t) + S_{cf}(t). \quad (A1)$$

The ''response time'' of the Pescadero watershed to changes in rain rate is roughly 2–3 h, based on the inspection of hydrographs and companion rain traces during a number of rain events. Furthermore, the decrease in runoff after the flood peak (i.e., the ''recession'') is typically significantly slower than its rise before the peak. This behavior is illustrated clearly in Fig. A1, showing four normalized runoff events, and a mean of these normalized events, on Pescadero Creek that led up to and included the 2–3 February 1998 flood. The asymmetry results from many causes, including the fact that runoff flows more slowly through the soil than above ground and that this subsurface flow continues to enter the stream and its tributaries even well after the rain stops. However, the recession rate can also vary significantly due to a number of other factors, including

---

[A1] Though the warm front moved northward beyond the Pescadero Creek drainage at ~2100 UTC 2 February (see Figs. 7a and 8a), for the purpose of simplifying the present discussion we consider the rainfall prior to 2200 UTC as warm frontal.
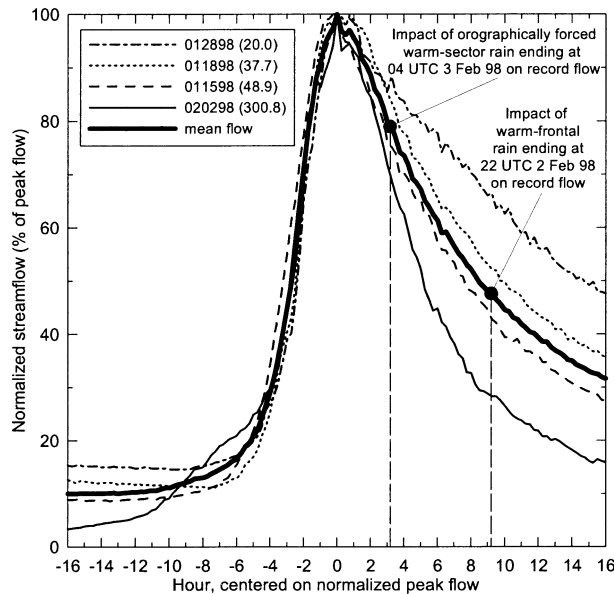
FIG. A1. Traces of normalized streamflow (% of peak flow) of four runoff events (thin curves) on Pescadero Creek just prior to and including the flood event of 2–3 Feb 1998. The starting month, day, and year of each trace is shown in the key, as is the peak flow magnitude (m³ s⁻¹; in parentheses). The mean of those traces (bold curve) is also shown. The normalized peak flow for each event is at hour = 0. The recession portion of the mean trace is marked with bold dots at hour = 3.25 and 9.25 to determine the impact of the warm-frontal rainfall and the 6-h period of orographically forced warm-sector rainfall on the record flow at Pescadero Creek at 0945 UTC 3 Feb 1998. Date of traces are in the form day day/month month/year year.

FIG. A2. The hydrograph trace from Pescadero Creek on 2–3 Feb 1998 [$S_{tot}(t)$; m³ s⁻¹; solid curve]. Dark shading between the dotted curves denotes the estimated contribution to the total streamflow due to the 6-h period of orographically forced warm-sector rain [$S_{ws}(t)$], and the light shading above the top dotted-curve and beneath the bottom dotted-curve mark the estimated contributions to the total streamflow due to the pre-cold-frontal and cold-frontal rain [$S_{cf}(t)$] and the warm-frontal rain [$S_{wf}(t)$], respectively. The X and its error bars denote the estimated peak streamflow that excludes the impact of the 6-h period of orographically forced warm-sector rain. The magnitude and ranking of the eight largest floods observed in Pescadero Creek are shown with bold dots and numbers, respectively. The gray-shaded vertical bar represents the key 6-h period within the warm sector, as in Fig. 7.

the direct dependence of the recession rate on the magnitude of the preceding peak flow (e.g., see Fig. A1), variable soil moisture content, and rainfall that continues after the primary event. The soil moisture conditions and rainfall characteristics associated with the four runoff events in Fig. A1 were similar. Specifically, the soil during each event was quite likely saturated, given that copious rain (325–533 mm) fell across the Santa Cruz Mountains during January 1998. In addition, heavy rain fell in advance of each runoff maximum, followed by an abrupt decrease in rain rate several hours prior to the maximum (not shown), thus approximating a sudden cessation of rainfall in each case.

Based on the soil conditions, which were either saturated or near saturation, and the abrupt cessation of rainfall that preceded the peak flow of the four runoff events, the receding portion of the mean normalized hydrograph in Fig. A1 can be viewed as a characteristic recession following significant storms for this basin during the exceptionally wet winter of 1997/98. Hence, this mean hydrograph is used to estimate the components of $S_{tot}(t)$, and to estimate the contribution of $S_{wf}(t)$ and $S_{ws}(t)$ to the record peak flow at t = 0945 UTC 3 February (see Fig. A2). Given the 2–3-h response time in Pescadero Creek to changes in rain rate, a 2.5-h time lag is used between the end of the warm-sector rainfall
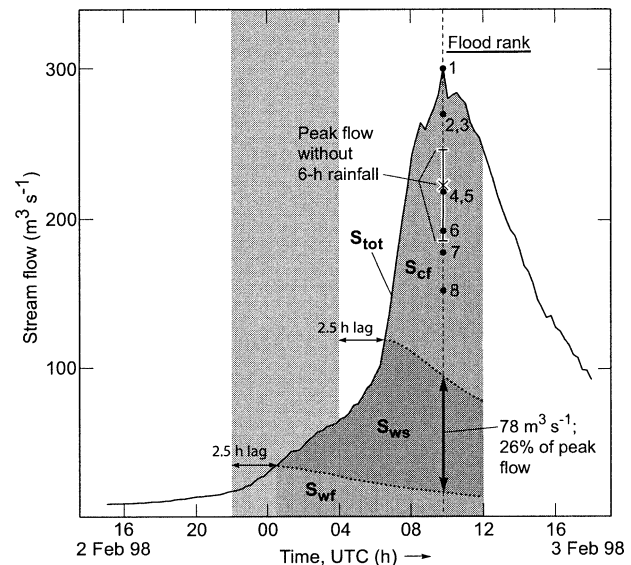
and the estimated initial streamflow recession associated with the end of this period of rainfall. The same time lag is used for the warm-frontal rainfall and its estimated runoff. As a result, the estimated streamflow attributed to the warm-frontal rain started receding at 0030 UTC 3 February (i.e., 9.25 h prior to the record peak flow; right bold dot in Fig. A1), and the estimated streamflow attributed to the combined warm-frontal/warm-sector rain began receding at 0630 UTC 3 February (i.e., 3.25 h before the record peak flow; left bold dot in Fig. A1). The recession characteristics of these estimated streamflow traces (see dotted curves in Fig. A2) were derived from the observed streamflow magnitudes at 0030 and 0630 UTC in conjunction with the receding portion of the mean normalized hydrograph in Fig. A1.

The estimated traces in Fig. A2 clearly show that the runoff associated with the heavy pre-cold-frontal and cold-frontal rains (S_{cf}) contributed dominantly to the record flood ranking at 0945 UTC. However, Fig. A2 also reveals that the contribution of S_{wf} to the record peak flow of 300.8 m³ s⁻¹ is 16.8 m³ s⁻¹. Similarly, the combined contribution of S_{wf} and S_{ws} to the record peak flow is 94.8 m³ s⁻¹. Hence, the runoff contribution to the record peak flow from the 6-h period of orographically forced warm-sector rainfall (S_{ws}) when the adja-

cent watershed was within a rain shadow is 78.0 m³ s⁻¹. This represents 26% of the record peak flow. To assess the uncertainty of this estimate of the contribution of S_{ws} to the record peak flow (i.e., to calculate the error bars in Fig. A2), the exercise described above was also carried out using the normalized runoff event with the smallest recession rate (012898 in Fig. A1) in conjunction with a 3-h lag, and the normalized runoff event with the fastest recession rate (020298 in Fig. A1) together with a 2-h lag. This approach yields a range for S_{ws} of 111.8 m³ s⁻¹ (37% of record peak flow) to 52.7 m³ s⁻¹ (18% of record peak flow), or 26 ± ~9% of the record peak flow.

Based on the range of estimates for S_{ws}, the hydrologic characteristics of Pescadero Creek are such that the period of rainfall between 2200 UTC 2 February and 0400 UTC 3 February contributed significantly to the generation of the record flood at 0945 UTC 3 February. If the minimum estimated contribution of S_{ws} were removed, it would have reduced the peak flood to the third highest on record, while removal of the maximum estimated contribution would have lowered it to the sixth-highest flood.[A2] This result supports the overall assertion that the orographically forced warm-sector rainfall caused the flooding in the sparsely populated Pescadero basin to attain record status. This is also consistent with the conclusion that the rain shadow played a key role in reducing the flooding and associated flood damage in the much more populous San Lorenzo basin.

APPENDIX B

The Downstream Drift of Rainfall in the Santa Cruz Mountains

The key parameters used to determine the downstream drift of the QPE field derived from the experimental Z–R relationship (Fig. 13a) are the low-level horizontal wind velocity, the hydrometeor fall speed, and the terrain slope and elevation. A 6-h-averaged horizontal wind velocity of 25.4 m s⁻¹ from 169° was measured by the coastal wind profiler at PPB in the 800-m-deep orographic controlling layer between 0.6 and 1.4 km MSL (see dark-gray-shaded rectangle in Fig. 9a). This mean measurement quite likely represented flow conditions impacting the western Santa Cruz Mountains, because the flow in both regions did not initially encounter upstream terrain, and because the mean low-level VAD wind observations from the MUX radar in the eastern Santa Cruz Mountains mirrored those at PPB (Fig. 11a). Therefore, the time-averaged, layer-mean wind velocity of 25.4 m s⁻¹ from 169° is used in the QPE-drift calculations. A wind profiler at NPS also provided lower-tropospheric wind data (Fig. 11a), but this site was sheltered <20 km downstream

of the Santa Lucia Mountains (Fig. 11b), resulting in weaker low-level flow than that observed at PPB and UMN.

Range–height reflectivity analyses constructed from MUX radar data during the 6-h period (not shown) indicate that a mixture of brightband rain and nonbrightband rain fell over the western Santa Cruz Mountains, though these scans could not provide measurements of the hydrometeor fall speeds. The experimental S-band radar northwest of San Francisco regularly observed both types of rainfall during CALJET. The seasonwide modal fall speeds measured by the experimental radar below ~1400 m MSL during brightband rain and nonbrightband rain were 6.25 and 2.25 m s⁻¹, respectively (White et al. 2003). Therefore, based on the assumptions that the 6-h window of warm-sector rainfall on 2–3 February consisted of coequal periods of brightband rain and nonbrightband rain, and that the precipitation microphysics were similar at each of these coastal mountain locations, the average fall speed over the Santa Cruz Mountains during this time was assumed to be 4.1 m s⁻¹.

The terrain slope in the western Santa Cruz Mountains and at the experimental S-band site was very similar (~8%). However, the strong low-level flow during the 6-h period on 2–3 February (25.4 m s⁻¹) was at least 50% greater than the average flow of 16.9 m s⁻¹ that occurred in conjunction with the seasonwide fall speed measurements. Therefore, orographically forced ascent was at least 50% or 0.7 m s⁻¹ larger in the Santa Cruz Mountains. Superimposing the additional orographically forced upward motion on the hydrometeor fall speeds measured at the experimental S-band radar yields a modified hydrometeor fall speed of 3.4 m s⁻¹.

The core of heavy warm-sector rainfall during the 6-h period was situated 23 km west of the MUX radar (1077 m MSL). At this range, the lower and upper bounds of the 0.5° radar beam extend from 31 to 433 m above the radar, or an average of 1309 m MSL. Given that the pass between the San Lorenzo and Pescadero watersheds is ~500 m MSL, and that a hydrometeor fall speed of 3.4 m s⁻¹ is assumed, it would take 238 s for the hydrometeors to fall 809 m before impacting the pass. This estimate predicts a total phase-shifted distance for the QPE field of 6.0 km from 169°. Based on a series of six correlation and root-mean-square error (rmse) analyses that compared the rain gauge observations in the domain of Fig. 13 to the QPE analysis for each of six advective phase shifts between 0 and 12.5 km at 2.5-km increments (Table B1), the 6.0-km shift was too small. Table B1 shows that a 7.5-km downstream drift best matches the rain gauge data. Drifts >12.5 km were not considered because it would have required unrealistic meteorological conditions.

Minor realistic adjustments to the meteorological parameters can account for an increase in the downstream drift from 6.0 to 7.5 km. For example, a 10% increase in the magnitude of the horizontal flow from 25.4 to

---

[A2] Removal of S_{wf} in either scenario would not have reduced the record flood ranking.

TABLE B1. Correlation (r^2) and root-mean-square error (rmse) as a function of the downstream drift (km) of the QPE field. The rms and r^2 values are based on comparisons between the observations of 6-h rainfall (dots in Fig. 13) and the radar-derived 6-h QPE field using the experimental Z–R relationship (color analysis in Fig. 13) for six different advective shifts from 0 to 12.5 km.

Advective shift of QPE field (km)	Rmse (mm) Obs vs QPE	Correlation (r^2) Obs vs QPE
0.0	6.48	0.49
2.5	5.47	0.62
5.0	5.07	0.68
7.5	4.29	0.78
10.0	4.41	0.76
12.5	4.56	0.77

27.9 m s^{-1} (supported by MUX radial velocity data) increases the downstream drift to 6.6 km. Decreasing the mean hydrometeor fall speed by 10%, easily within the range of values possible for a mix of nonbrightband and brightband rain, to 3.06 m s^{-1} increases the downstream drift to 7.4 km, consistent with the results in Table B1. The strong low-level winds, combined with the relatively small hydrometeor fall velocities, indicate that this case was especially susceptible to a significant downstream drift of rainfall from one watershed to the next.

The mean bias between the observed 6-h rainfall and the QPE field for the six phase shifts is −0.6 mm for the experimental Z–R relationship and −4.5 mm for the default Z–R relationship. The default relationship significantly underestimated the rainfall because it assumes larger drop sizes than have been inferred in California's coastal mountain precipitation (e.g., White et al. 2003). Thus, the QPE field derived from the experimental Z–R relationship was used.

REFERENCES

Andrews, E. D., R. C. Antweiler, P. J. Neiman, and F. M. Ralph, 2004: Influence of ENSO on flood frequency along the California coast. *J. Climate,* **17**, in press.

Barnston, A. G., A. Leetmaa, V. E. Kousky, R. E. Livezey, E. A. O'Lenic, H. Van den Dool, A. J. Wagner, and D. A. Unger, 1999: NCEP forecasts of the El Niño of 1997–98 and its U.S. impacts. *Bull. Amer. Meteor. Soc.,* **80**, 1829–1852.

Brady, R. H., and J. S. Waldstreicher, 2001: Observations of mountain wave–induced precipitation shadows over northeast Pennsylvania. *Wea. Forecasting,* **16**, 281–300.

Browning, K. A., and R. Wexler, 1968: The determination of kinematic properties of a wind field using Doppler radar. *J. Appl. Meteor.,* **7**, 105–113.

——, F. F. Hill, and C. W. Pardoe, 1974: Structure and mechanism of precipitation and the effect of orography in a wintertime warm sector. *Quart. J. Roy. Meteor. Soc.,* **100**, 309–330.

Carlson, T. N., 1991: *Mid-Latitude Weather Systems.* Harper Collins, 507 pp.

Cayan, D. R., and R. H. Webb, 1992: El Niño/Southern Oscillation and streamflow in the western United States. *Historical and Paleoclimate Aspects of the Southern Oscillation,* H. F. Diaz and V. Markgraf, Eds., Cambridge University Press, 29–68.

——, K. T. Redmond, and L. G. Riddle, 1999: ENSO and hydrologic extremes in the western United States. *J. Climate,* **12**, 2881–2893.

Charba, J. P., D. W. Reynolds, B. E. McDonald, and G. M. Carter, 2003: Comparative verification of recent quantitative precipitation forecasts in the National Weather Service: A simple approach for scoring forecast accuracy. *Wea. Forecasting,* **18**, 161–183.

Chien, F.-C., C. F. Mass, and P. J. Neiman, 2001: An observational and numerical study of an intense landfalling cold front along the northwest coast of the United States during COAST IOP 2. *Mon. Wea. Rev.,* **129**, 934–955.

Crum, T. D., R. L. Alberty, and D. W. Burgess, 1993: Recording, archiving, and using WSR-88D data. *Bull. Amer. Meteor. Soc.,* **74**, 645–653.

Dettinger, M. D., D. R. Cayan, H. F. Diaz, and D. M. Meko, 1998: North–south precipitation patterns in western North America on interannual to decadal timescales. *J. Climate,* **11**, 3095–3111.

Doyle, J. D., 1997: The influence of mesoscale orography on a coastal jet and rainband. *Mon. Wea. Rev.,* **125**, 1465–1488.

Ecklund, W. L., D. A. Carter, and B. B. Balsley, 1988: A UHF wind profiler for the boundary layer: Brief description and initial results. *J. Atmos. Oceanic Technol.,* **5**, 432–441.

Fulton, R. A., J. P. Breidenbach, D.-J. Seo, D. A. Miller, and T. O'Bannon, 1998: The WSR-88D rainfall algorithm. *Wea. Forecasting,* **13**, 377–395.

Heggli, M. F., and R. M. Rauber, 1988: The characteristics and evolution of supercooled water in wintertime storms over the Sierra Nevada: A summary of microwave radiometric measurements taken during the Sierra Cooperative Pilot Project. *J. Appl. Meteor.,* **27**, 989–1015.

Hill, F. F., 1983: The use of average annual rainfall to derive estimates of orographic enhancement of frontal rain over England and Wales for different wind directions. *J. Climatol.,* **3**, 113–129.

——, and K. A. Browning, 1979: Persistence and orographic modulation of mesoscale precipitation areas in a potentially unstable warm sector. *Quart. J. Roy. Meteor. Soc.,* **105**, 57–70.

Houze, R. A., 1993: *Cloud Dynamics.* Academic Press, 570 pp.

Jorgensen, D. P., 1984: Mesoscale and convective-scale characteristics of mature hurricanes. Part I: General observations by research aircraft. *J. Atmos. Sci.,* **41**, 1268–1285.

——, T. Matejka, and J. D. DuGranrut, 1996: Multi-beam techniques for deriving wind fields from airborne Doppler radars. *J. Meteor. Atmos. Phys.,* **59**, 83–104.

Kahya, E., and J. A. Dracup, 1994: The influences of Type 1 El Niño and La Niña events on streamflows in the Pacific southwest of the United States. *J. Climate,* **7**, 965–976.

Kalnay, E., and Coauthors, 1996: The NCEP/NCAR 40-Year Reanalysis Project. *Bull. Amer. Meteor. Soc.,* **77**, 437–471.

Klazura, G. E., and D. A. Imy, 1993: A description of the initial set of analysis products available from the NEXRAD WSR-88D system. *Bull. Amer. Meteor. Soc.,* **74**, 1293–1311.

Linsley, R. K., Jr., M. A. Kohler, and J. L. H. Paulhus, 1986: *Hydrology for Engineers.* McGraw-Hill, 508 pp.

Livezey, R. E., M. Masutani, A. Leetmaa, H. Rui, M. Ji, and A. Kumar, 1997: Teleconnective response of the Pacific–North American region atmosphere to large central equatorial Pacific SST anomalies. *J. Climate,* **10**, 1787–1820.

Lowndes, S., 1968: Forecasting large 24-h rainfall totals in the Dee and Clwyd River Authority Area from September to February. *Meteor. Mag.,* **97**, 226–235.

Marwitz, J. D., 1987: Deep orographic storms over the Sierra Nevada. Part I: Thermodynamic and kinematic structure. *J. Atmos. Sci.,* **44**, 159–173.

Mendell, T., 1992: Integration of automated hydrological data. Preprints, *Conf. on Interdisciplinary Approaches in Hydrology and Hydrogeology,* Portland, OR, American Society of Civil Engineers.

NCDC, 1998: *Storm Data,* Vol. 40, No. 2. National Climatic Data Center, 188 pp.

Neiman, P. J., F. M. Ralph, A. B. White, D. E. Kingsmill, and P. O. G. Persson, 2002: The statistical relationship between upslope

flow and rainfall in California's coastal mountains: Observations during CALJET. *Mon. Wea. Rev.,* **130,** 1468–1492.

Nieman, S. J., W. P. Menzel, C. M. Hayden, D. Gray, S. T. Wanzong, C. S. Velden, and J. Daniels, 1997: Fully automated cloud-drift winds in NESDIS operations. *Bull. Amer. Meteor. Soc.,* **78,** 1121–1133.

Nuss, W. A., and D. K. Miller, 2001: Mesoscale predictability under various synoptic regimes. *Nonlinear Processes Geophys.,* **8,** 429–438.

Overland, J. E., and N. A. Bond, 1995: Observations and scale analysis of coastal wind jets. *Mon. Wea. Rev.,* **123,** 2934–2941.

Parish, T. R., 1982: Barrier winds along the Sierra Nevada mountains. *J. Appl. Meteor.,* **21,** 925–930.

Parsons, D. B., 1992: An explanation for intense frontal updrafts and narrow cold-frontal rainbands. *J. Atmos. Sci.,* **49,** 1810–1825.

Persson, P. O. G., P. J. Neiman, F. M. Ralph, B. Walter, J.-W. Bao, S. Michelson, D. Jorgensen, and J. Schmidt, 1999: Measurements and modeling of air–sea interaction processes prior to heavy coastal precipitation: The case of 3 February 1998. Preprints, *Third Conf. on Coastal Atmospheric and Oceanic Prediction and Processes,* New Orleans, LA, Amer. Meteor. Soc., 374–379.

Rabin, R., and D. Zrnić, 1980: Subsynoptic-scale vertical wind revealed by dual Doppler radar and VAD analysis. *J. Atmos. Sci.,* **37,** 644–654.

Ralph, F. M., and Coauthors, 1999: The California Land-Falling Jets Experiment (CALJET): Objectives and design of a coastal atmosphere–ocean observing system deployed during a strong El Niño. Preprints, *Third Symp. on Integrated Observing Systems,* Dallas, TX, Amer. Meteor. Soc., 78–81.

Rasmusson, E. M., 1985: El Niño and variations in climate. *Amer. Sci.,* **73,** 168–177.

——, and J. M. Wallace, 1983: Meteorological aspects of the El Niño/Southern Oscillation. *Science,* **222,** 1195–1202.

Reynolds, D. W., and A. P. Kuciauskas, 1988: Remote and in situ observations of Sierra Nevada winter mountain clouds: Relationships between mesoscale structure, precipitation, and liquid water. *J. Appl. Meteor.,* **27,** 140–156.

Rhea, J. O., 1978: Orographic precipitation model for hydrometeo-rological use. Ph.D. dissertation, Colorado State University, 198 pp.

Schonher, T., and S. E. Nicholson, 1989: The relationship between California rainfall and ENSO events. *J. Climate,* **2,** 1258–1269.

Smith, R. B., 1979: The influence of mountains on the atmosphere. *Advances in Geophysics,* Vol. 21, Academic Press, 87–230.

——, and Coauthors, 1997: Local and remote effects of mountains on weather: Research needs and opportunities. *Bull. Amer. Meteor. Soc.,* **78,** 877–892.

Velden, C. S., C. M. Hayden, S. J. Nieman, W. P. Menzel, S. Wanzong, and J. S. Goerss, 1997: Upper-tropospheric winds derived from geostationary satellite water vapor observations. *Bull. Amer. Meteor. Soc.,* **78,** 173–195.

Webb, R. H., and J. L. Betancourt, 1992: Climate variability and flood frequency of the Santa Cruz River, Pima County, Arizona. U.S. Geological Survey Water-Supply Papers 2379, 40 pp.

Weber, B. L., D. B. Wuertz, D. C. Welsh, and R. McPeek, 1993: Quality controls for profiler measurements of winds and RASS temperatures. *J. Atmos. Oceanic Technol.,* **10,** 452–464.

Wentz, F. J., 1997: A well-calibrated ocean algorithm for special sensor microwave/imager. *J. Geophys. Res.,* **102,** 8703–8718.

Westrick, K. J., C. F. Mass, and B. A. Colle, 1999: The limitations of the WSR-88D radar network for quantitative precipitation measurement over the coastal western United States. *Bull. Amer. Meteor. Soc.,* **80,** 2289–2298.

White, A. B., P. J. Neiman, F. M. Ralph, D. E. Kingsmill, and P. O. G. Persson, 2003: Bulk microphysical characteristics of rainfall observed at a California coastal mountain site during CALJET. *J. Hydrometeor.,* **4,** 264–282.

Wolter, K., and M. S. Timlin, 1993: Monitoring ENSO in LOADS with a seasonally adjusted principal component index. *Proc. 17th Climate Diagnostics Workshop,* Norman, OK, NOAA/CAC, 52–57.

——, and ——, 1998: Measuring the strength of ENSO events: How does 1997/98 rank? *Weather,* **53,** 315–324.

Yu, C.-H., and B. F. Smull, 2000: Airborne Doppler observations of a landfalling cold front upstream of steep coastal orography. *Mon. Wea. Rev.,* **128,** 1577–1603.